Athalye *et al.*
Acta Neuropathologica Communications (2025) 13:120
https://doi.org/10.1186/s40478-025-02030-y

Acta Neuropathologica
Communications

RESEARCH **Open Access**

Operationalizing postmortem pathology-MRI association studies in Alzheimer's disease and related disorders with MRI-guided histology sampling

Chinmayee Athalye[1*], Alejandra Bahena[2], Pulkit Khandelwal[1], Sheina Emrani[2], Winifred Trotman[2], Lisa M. Levorse[3], Zahra Khodakarami[1], Daniel T. Ohm[2], Eric Teunissen-Bermeo[2], Noah Capp[2], Shokufeh Sadaghiani[2], Sanaz Arezoumandan[2], Sydney A. Lim[3], Karthik Prabhakaran[2], Ranjit Ittyerah[3], John L. Robinson[4], Theresa Schuck[4], Edward B. Lee[4], M. Dylan Tisdall[3], Sandhitsu R. Das[2], David A. Wolk[2], David J. Irwin[2] and Paul A. Yushkevich[3]

Abstract

Postmortem neuropathological examination, while the gold standard for diagnosing neurodegenerative diseases, often relies on limited regional sampling that may miss critical areas affected by Alzheimer's disease and related disorders. Ultra-high resolution postmortem MRI can help identify regions that fall outside the diagnostic sampling criteria for additional histopathologic evaluation. However, there are no standardized guidelines for integrating histology and MRI in a traditional brain bank. We developed a comprehensive protocol for whole hemisphere postmortem 7T MRI-guided histopathological sampling with whole-slide digital imaging and histopathological analysis, providing a reliable pipeline for high-volume brain banking in heterogeneous brain tissue. Our method uses patient-specific 3D printed molds built from postmortem MRI, allowing standardized tissue processing with a permanent spatial reference frame. To facilitate pathology-MRI association studies, we created a semi-automated MRI to histology registration pipeline and developed a quantitative pathology scoring system using weakly supervised deep learning. We validated this protocol on a cohort of 29 brains with diagnosis on the AD spectrum that revealed correlations between cortical thickness and phosphorylated tau accumulation. This pipeline has broad applicability across neuropathological research and brain banking, facilitating large-scale studies that integrate histology with neuroimaging. The innovations presented here provide a scalable and reproducible approach to studying postmortem brain pathology, with implications for advancing diagnostic and therapeutic strategies for Alzheimer's disease and related disorders.

Keywords Alzheimer's disease, Postmortem imaging, Histology, Quantitative pathology, MRI-histology registration

Introduction

Neurodegenerative diseases are a clinically and pathologically heterogeneous group of disorders characterized by distinct protein aggregates such as amyloids, tau, α-synuclein, and TDP-43 [1, 2]. Obtaining a molecular diagnosis of underlying pathologies in living patients is challenging due to frequent co-occurrence of multiple pathologies, clinical convergence of disparate pathologies within the

---

*Correspondence:
Chinmayee Athalye
cathalye@seas.upenn.edu
[1] Department of Bioengineering, University of Pennsylvania, Philadelphia, USA
[2] Department of Neurology, University of Pennsylvania, Philadelphia, USA
[3] Department of Radiology, University of Pennsylvania, Philadelphia, USA
[4] Department of Pathology and Laboratory Medicine, University of Pennsylvania, Philadelphia, USA

same clinical syndrome (e.g. frontotemporal dementia due to tau or TDP-43 pathology) and a lack of established biomarkers for some forms of neurodegenerative disorders that can be detected in vivo [3, 4]. As such, autopsy remains the gold standard to confirm the underlying distinct pathologies. Understanding the neuropathological pathways, interactions, and clinical manifestations of these co-pathologies is crucial to developing targeted therapies [5] for specific disorders such as Alzheimer's disease (AD) [6], frontotemporal dementia (FTD) [7], Parkinson's Disease [8], Lewy body disease (LBD) [2], limbic predominant age-related TDP-43 encephalopathy (LATE) [9], small vessel disease (SVD) [10], etc. Moreover, neurodegenerative dementias affect large scale neurocognitive networks and complex human behaviors that are difficult to study in animal/cell models, making it essential to have human brain tissue samples for representative studies of their natural progression and effects. Hence, brain banks are a vital resource that provide access to high quality, donated postmortem brain tissue samples for Alzheimer's disease and related dementia (ADRD) research [11, 12].

Digital histopathology of the brain tissue enables us to study diseases on a cellular level [13]. We can use dedicated stains that specialize in delineating cytoarchitectural structures with high contrast or use specific antibodies to study certain proteins and molecules in great detail. This has accelerated advances in knowledge about etiology and underlying pathological mechanisms of a range of diseases [14–16]. However, histology is inherently a two-dimensional imaging modality and limited in thickness of a given sample for histopathological staining, necessitating time and resource intensive stereological method to examine depth of tissue that are prohibitive for a whole-hemisphere approach. Magnetic Resonance Imaging (MRI) is an important, non-invasive imaging method that is used to diagnose and track the progression of various neurodegenerative diseases in vivo [17]. MRI allows us to study the brain while preserving its three-dimensional structure. However, standard clinical MRI protocols imaged at 1.5T and 3T (0.5 to 1 mm^3 resolution) are not sufficient to understand the pathology on a deeper level. Ex vivo (postmortem) MRI benefits from extended scanning time without significant motion artifacts and high signal-to-noise ratio [18]. Ex vivo MRI imaging performed at 7T gives higher spatial resolution (0.16 to 0.3 mm^3) and is capable of laminar resolution while also preserving the gross anatomic orientation of the brain regions [19, 20]. Together, MRI and histology provide complementary insights about disease pathways [21], with MRI offering morphometric information while histology reveals the cellular details of tissue pathology for direct radiographic-pathological correlation and validation. Ex vivo MRI provides us with the brain scan at a time point closer to the when the histological sampling is done versus antemortem MRI scan which might be done months or years prior to the histopathological assessment [22]. The long delay between antemortem MRI and histology processing can weaken MRI-pathology correlations due to potential of untracked pathological changes in the interim. Nonetheless we have correlated antemortem MRI measurements with corresponding postmortem digital pathology data within the same subjects while carefully accounting for disease duration from MRI to autopsy [23–27]. Thus, ex vivo MRI guided histopathology provides a critical means of bridging the gap between antemortem imaging and histology on the macroscale. Specifically in ADRD, previous works have mapped the neurofibrillary tangle burden in the medial temporal lobe (MTL) [16], studied the relationship of cortical thickness measurements in ex vivo MRI to amount of phosphorylated tau [28], and studied differences in tau and TDP-43 pathology [29].

Linked MRI and histology studies are fundamental to studying neurodegenerative diseases on a micro and macro scale [30]. Beyond histopathological validation of radiological findings, these studies are key to developing non-invasive imaging biomarkers for a differential diagnosis of diseases [22]. But there are a number of challenges that prevent scaling up these multi-modal imaging pipelines. Processing brain tissue for histology is a resource-intensive task. Traditional stereology using serial histology (e.g. with sections acquired every 500 μm as in [16] or every 250 μm for denser protocols as in [31]) makes it possible to reconstruct histological images in 3D. Assuming a brain hemisphere to span 20 cm, this would mean generating at least hundreds, if not thousands, of slides for each hemisphere [19] to build a complete histological picture and additional immunohistochemical processing which would take months. Previous studies that have used stereology were either in a small region such as the MTL [16] or only used two to five subjects for whole hemispheres [19, 31]. Moreover, thicker tissues often require free-floating staining methods which utilize a large amount of antibody and reagents, which precludes large-scale work. On the other hand, in the absence of serial histology, registration (accurate alignment) of histology to MRI is an extremely challenging problem. For larger brain areas, the tissue may be cut into several segments to fit the blocks on histology slides, which makes it a part-to-whole registration challenge [32]. Registration is made further difficult by the disparate nature of the two modalities. There are large differences in the contrast and resolution of MRI and histology - depending on the stain used, histology may not always shows clear boundaries between white matter and gray matter that are a distinct feature of MRI. Fixation and embedding steps, done before histological processing, cause non-uniform shrinkage of the tissue. Cutting and sectioning this paraffin-embedded block introduces further distortions like cuts and folds in the tissue. Previous works have used serial histology for 3D histological reconstruction of the brain and then registered this to the 3D ex vivo MRI [16, 33, 34]. However, for a sparse sampling scheme, it becomes a 2D histology to 3D MRI registration problem in addition to all the existing challenges [35].

Despite the established importance of linked postmortem MRI and histology studies in ADRD research, there are no standard guidelines for neuropathology researchers to process and integrate postmortem imaging in their research pipeline [36]. Until recently, most brain banks did not collect ex vivo MRI, making it an understudied approach [11, 37]. Traditional brain banking has relied on sparse diagnostic histological sampling from tissue blocks extracted from the brain at the time of autopsy. Neuropathological assessment of diagnostic samples is usually done in semi-quantitative manner where severity scores are assigned by visual inspection by expert raters [28, 38]. Semi-quantitative ratings do not fully capture the extent and load of pathology, nor do they typically distinguish between different types of pathology such as neurofibrillary tau threads and tau tangles, and manual ratings suffer from inter and intra-rater variability. Thus, digital histopathology has proven to be an effective means for performing more fine grained clinical and radiographic correlation studies but lacks standardization. We present a reproducible pipeline integrating ex vivo MRI and MRI-guided quantitative histopathology in high volume brain banking to acquire reliable data for linked morphometry and pathology correlation studies [30].

Our center has developed a high-throughput, ultra-high resolution whole hemisphere MRI scanning protocol [29] that involves scanning intact brain hemisphere in every brain donation after 60 days of formalin fixation with low occurrence of MRI inhomogeneity artifacts due to air bubbles and other factors. The ability to establish homologies between locations on these MRI scans and histopathology measures is critical for conducting studies that associate 3D MRI features such as volume, thickness, and texture changes in brain structures to pathologies, and through such studies, improving MRI-based biomarkers that address ADRD pathologic heterogeneity. In this work, we introduce our whole hemisphere MRI-guided histology sampling protocol that can be used for any general study of brain disorders. The workflow overview is shown in Fig. 1. We label cortical landmarks which are prospective histological sampling locations in the ex vivo MRI and use a patient-specific 3D printed mold created from the MRI scan to guide the sampling for histology. The mold acts as a frame of reference for initializing the MRI to histology registration process. Following standard histological tissue processing, the resulting formalin-fixed, paraffin-embedded (FFPE) blocks can be stored indefinitely at room temperature with no extra equipment. Thus, our methods are flexible to facilitate a relatively high-throughput whole-hemisphere histology sampling at 1 cm intervals in our 50×75 mm slides at 30 μm thickness, while the preserved FFPE block permits a traditional stereologic approach with serial sections in select regions of interest for future studies. We section the FFPE blocks that contain a region of interest using a standard microtome. We section at 30 μm thickness for greater resolution of cytoarchitectural structure and optimized on-slide immunohistochemistry to avoid laborious and cost-prohibitive free-floating staining methods. Whole-slide images are acquired from each section with meta-data stored in unique barcodes for each slide. The images are uploaded to our custom-built open-source archive (PICSL histology annotation server, or PHAS) that allows for collaboration and data sharing across research centers. Whole hemisphere MRI is then iteratively registered to the histology slides sampled from the regions containing the cortical landmarks. This registration provides us the region of interest on the histology tissue which can be studied in greater detail for neuropathology. We also introduce our quantitative pathology scoring scheme using a weakly supervised deep learning algorithm and demonstrate a use case of our pipeline for studying association of phosphorylated tau with

(See figure on next page.)

Fig. 1 Workflow for MRI-guided histological sampling. T2-weighted and CISS protocl scans of the hemisphere are obtained using a 7T MRI scanner. Green box shows the steps involved in histological processing of the hemisphere. The hemisphere is cut into uniform 1 cm thick slab using a 3D printed mold created from the hemisphere segmentation. Slabs containing cortical landmarks of interest (obtained from the corresponding MRI scan) are processed for histological sectioning and staining. We use standard anatomical stains like LFB-CV and H&E and anti-tau AT-8 immunohistochemistry stain for all sections. Blue box shows the steps in processing the T2-weighted MRI scan. Cortical landmarks are marked on the hemisphere and then the hemisphere is virtually slabbed into uniform 1 cm thick slabs. This virtual slabbing tells us the slabs that contain the cortical landmarks. Only those corresponding slabs are processed for histology. Orange box shows the registration pipeline. Either LFB-CV or H&E stain is chosed as the reference slide. MRI and remaining histology slides are both registered to the reference slide. The result of the registration gives us the location of the cortical landmarks on the histology slides

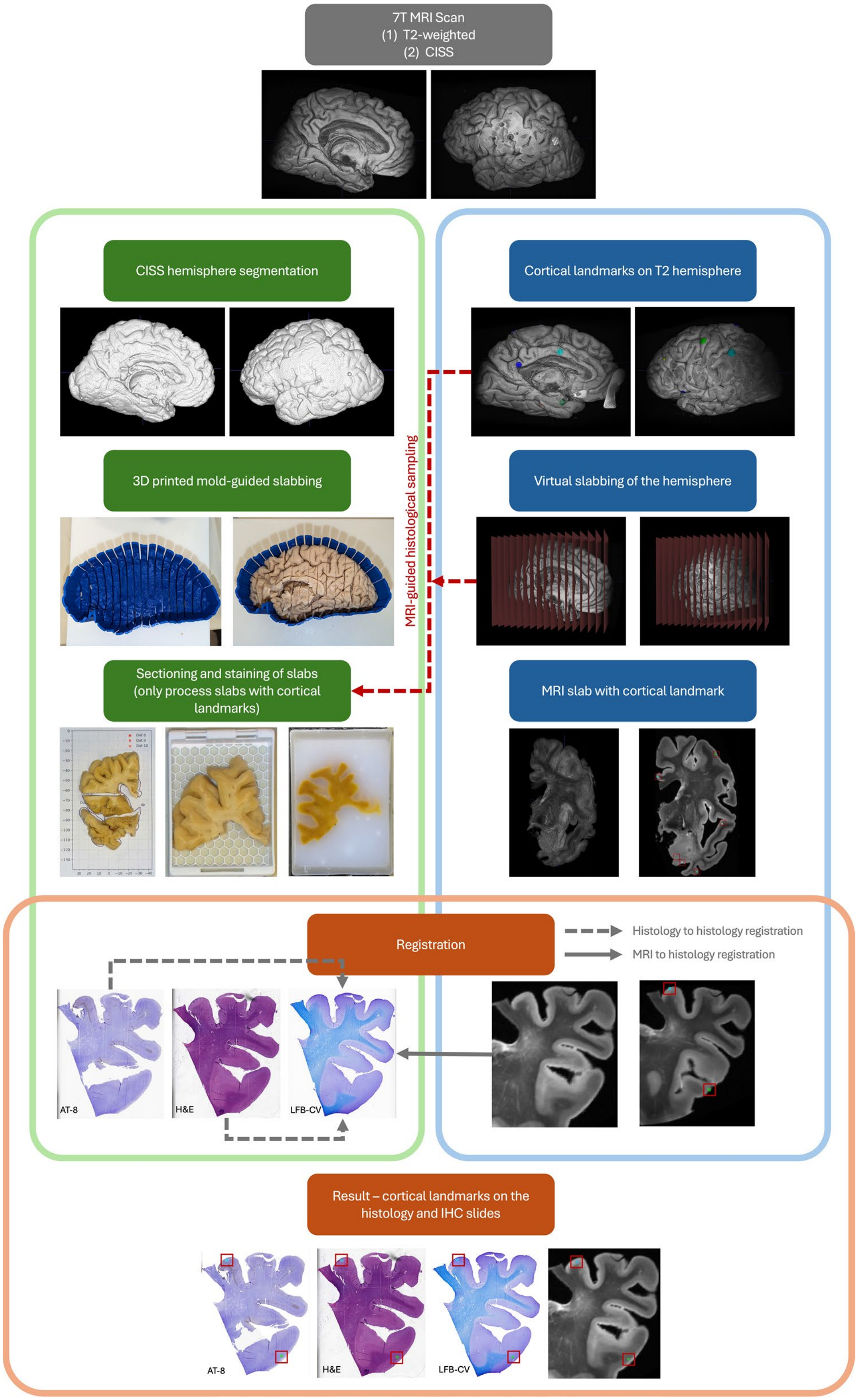

Fig. 1 (See legend on previous page.)

cortical thickness with both measurements obtained from homologous locations in the same hemisphere.

Methods

In this section, we describe the MRI-guided histological sampling protocol followed by the registration methods, and lastly introduce our weakly supervised deep learning algorithm for quantitative scoring of pathology in digital histology.

Data acquisition

Patients were followed clinically and invited to participate in the brain donation program by the University of Pennsylvania's Alzheimer's Disease Core Center, the Penn Memory Center, the Frontotemporal Degeneration Center, the ALS center, the Parkinson's Disease and Movement Disorder Clinic, and the Penn Udall Center for Parkinson's Research. Brain autopsies were performed at the University of Pennsylvania Center for Neurodegenerative Disease Research. The multidimensional data collected under the biobank protocols is stored in the Integrated Neurodegenerative Disease Database (INDD) as described previously [39]. All participants agreed to participate in the research study according to the University of Pennsylvania Institutional Review Board and the the next-of-kin provided consent for autopsy.

One hemisphere was used for diagnostic sampling and neuropathological analysis which involved staining with antibodies for detection of abnormal proteins following the NIA-AA protocol [38]. In AD patients, this included a random mix of right and left hemispheres. Since FTD is often asymmetric, we choose the most atrophic hemisphere for imaging (e.g. left hemisphere for primary progressive aphasia) and performed small in situ sampling with uniform fixation from up to 15 regions [25] which facilitated inter-hemispheric comparisons [25, 26] with standard uniform fixed 25×75 mm sections while preserving the intact hemisphere for ex vivo MRI. These samples were reviewed by board-certified neuropathologists and assigned semi-quantitative pathological scores in each diagnostic region. The remaining tissue from the diagnostic hemisphere is frozen at -80° C for biochemical studies [39]. The other hemisphere was fixed in 10% neutral buffered formalin for at least 60 days prior to further imaging.

MRI imaging

Our center has successfully implemented a high-throughput, ultra-high resolution, whole hemisphere MRI scanning protocol. Over the last 4 years, we have scanned over 125 brain hemispheres using this protocol. Hemispheres were placed in Fomblin (California Vacuum Technology; Fremont, CA), an MRI-neutral recycled industrial oil, and scanned using a 7T scanner (MAGNETOM Terra, Siemens Healthineers; Erlangen, Germany). The acquisition protocol included 3D-encoded T2-weighted sequence with 3 s repetition time (TR), 383 ms echo time (TE), turbo factor of 188, echo train duration of 951 ms, bandwidth of 348 Hz/px with four averages, and providing 0.28 mm^3 isotropic resolution in approximately 2 h. The vendor's on-scanner correction was applied during reconstruction to correct global frequency drift, merge signal averages in k-space, and generate magnitude images for each echo. We obtained 4 repeated measurements and averaged them to generate the final image [40].

In larger hemispheres, there was common signal dropout at the poles in the T2 sequence, as shown in Fig. 2a and 2b, which made it difficult to obtain a clear segmentation of the tissue in these regions. To overcome this problem, we used the Constructive Interference in Steady State (CISS) protocol, shown in Fig. 2d, to obtain a better SNR at the poles which gives an excellent contrast between the tissue and the background. Following the T2 acquisition, in the same scanning session, we performed a 3D-encoded CISS scan sequence with 7.8 ms TR, 3.9 ms TE, bandwidth of 302 Hz/px, and providing 0.5 mm^3 isotropic resolution in approximately 9 min.

Labeling cortical landmarks: On the 3D hemisphere segmentation, we marked the following 18 cortical landmarks by placing a 3×3×3 voxel dot - orbitofrontal gyrus, middle frontal gyrus, anterior cingulate gyrus, posterior cingulate gyrus, motor cortex, primary visual cortex, superior temporal gyrus, inferior temporal gyrus, inferior frontal cortex (Broca's area), insular gyrus, temporal pole, angular gyrus, superior parietal lobule, entorhinal cortex, Broadmann Area 35 (BA35), Cornu Ammonis 1 (CA1), subiculum, and parahippocampal cortex. These regions were selected based on the areas typically sampled by neuropathologists for AD pathology and importance for ADRD symptoms [41]. The landmarks were marked by a manual labeler in ITK-SNAP [42]. The landmarks are shown in Fig. 3 and the detailed standard operating procedure (SOP) for annotating them is included in the supplementary material.

3D printing hemisphere mold: The CISS scan was rigidly registered to the T2 scan using ITK-SNAP to correct any residual settling of the hemisphere between the two scans. For the CISS scan, a 3D tissue mask was created by segmenting the tissue voxels from the background using the semi-automated segmentation module from ITK-SNAP [43]. We created a custom, open-source software[1]

---

[1] https://github.com/pyushkevich/brainmold.

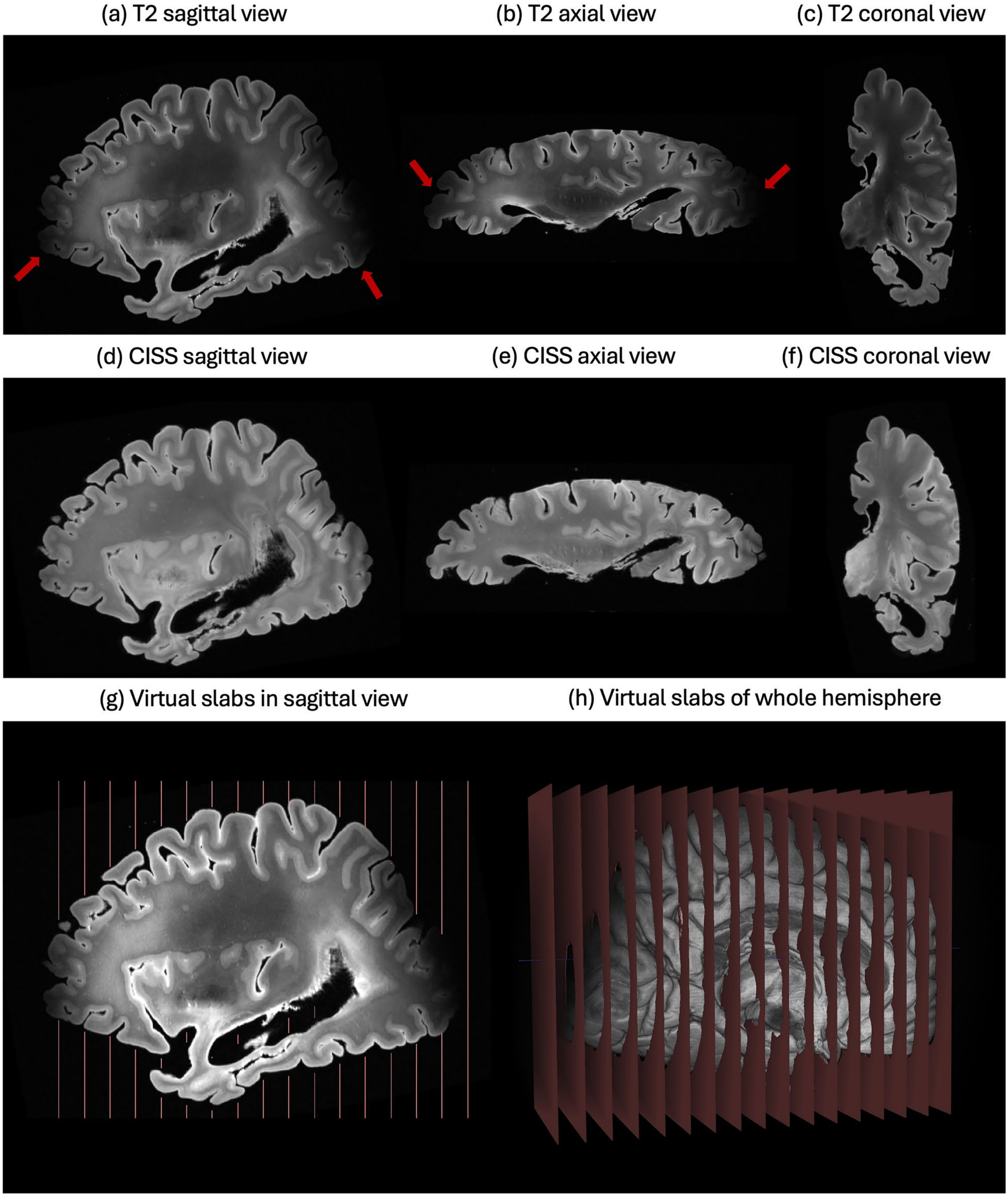

Fig. 2 MRI acquisition protocols and virtual slabs. We used two different protocols during MRI scanning for this pipeline. **a**, **b**, **c** We obtained a high-resolution T2-weighted sequence that was used for labeling cortical landmarks and obtaining cortical thickness measurements. However, there was common signal dropout at the poles as shown in (**a**) and (**b**) which made it difficult to obtain a clear segmentation. **d**, **e**, **f** Constructive Interference in Steady State (CISS) protocol overcomes this issue and provides excellent contrast between tissue and background. We use this scan to generate a complete 3D segmentation of the tissue. **g**, **h** Virtual slabs used to create a frame of reference between the 3D hemisphere scan and histology tissue blocks. The red lines correspond to the cuts made in the brain tissue using a 3D printed mold

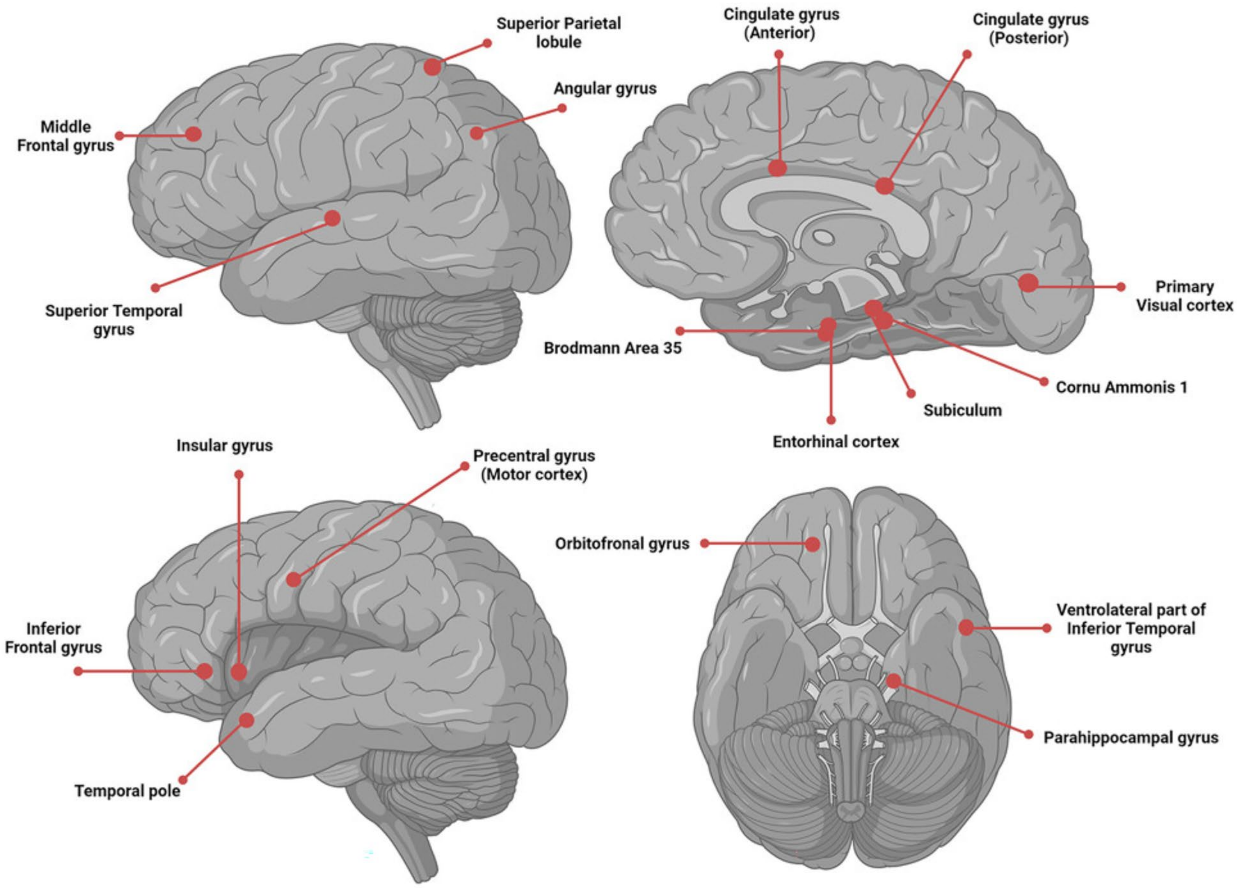

Fig. 3 Cortical landmarks. The 18 regions of interest were used to guide the histological sampling. We obtained cortical thickness measurements at all these landmarks. The MRI-guided histology protocol was used to obtain quantitative pathology scores at these locations to facilitate pathology-morphometry association studies. Figure adopted from [28] with permission

using Insight Toolkit (ITK), Visualization Toolkit (VTK), and standard C++ libraries to create 3D printable molds from the hemisphere MRI. The 3D printed mold has notches at every 1 cm which were used to guide the knife during cutting as shown in Fig. 4e. This ensured parallel cuts and coronal slabs of uniform thickness. The mold also established a reference system to know the plane of histology section relative to the whole hemisphere MRI. This helped with initializing the MRI to histology registration. The mold was printed using Ultimaker 3 Extended 3D printer (Ultimaker B.V.; Utrecht, The Netherlands).

Virtually, we also divided the 3D hemisphere segmentation into corresponding 1 cm thick coronal slabs as shown in Fig. 2h. We documented the distance of the cortical landmark label dots from the anterior and posterior of each 1 cm thick slab face. Since each coronal slab tissue would be cut starting from the anterior face for histological staining, we ensured that the dots were placed as anterior to the slab face as possible. We generated a printout with the outline of each slab and marked the positions of the label dots, as shown in Fig. 5a, that would be used as reference while slabbing the tissue.

MRI cortical landmarks-guided histological processing

To make the subsequent sections easier to follow, we use the following terminology: **slab** is the 1 cm thick coronal slab of brain tissue cut using the 3D printed mold; if a slab was cut into multiple parts, a **segment** refers to the part (superior, middle, or inferior); **block** refers to the processed and paraffin-embedded slab; **section** is the 30 μm thick piece of the block cut using a microtome; **slide** refers to a section mounted on a glass slide.

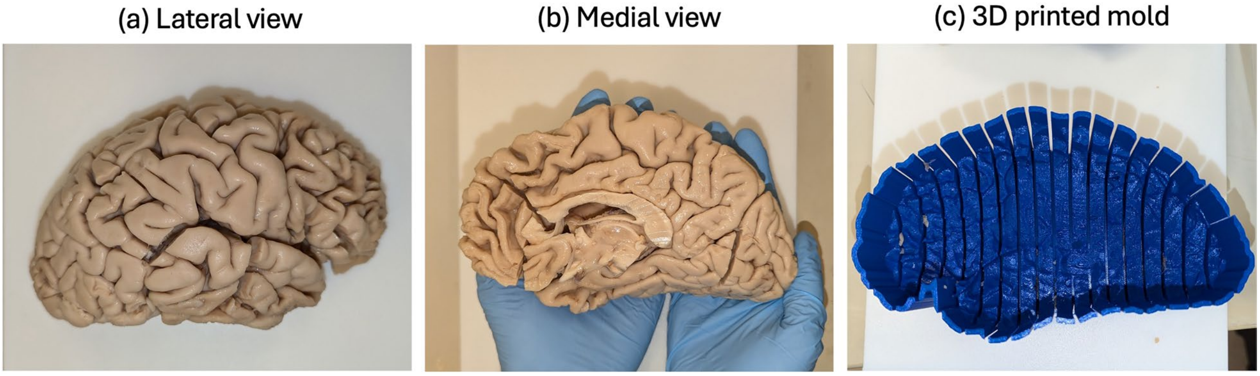
(a) Lateral view

(b) Medial view

(c) 3D printed mold

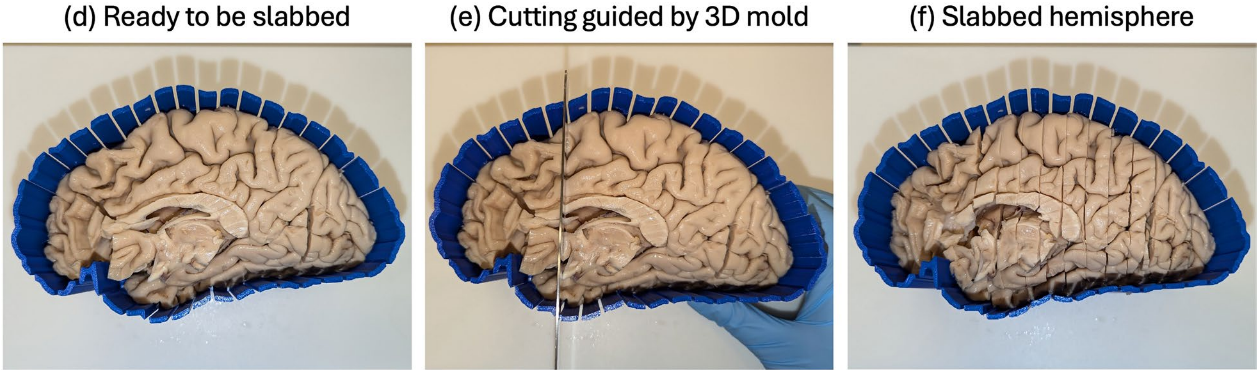
(d) Ready to be slabbed

(e) Cutting guided by 3D mold

(f) Slabbed hemisphere

Fig. 4 Custom 3D printed mold-guided slabbing of brain hemisphere. Postmortem whole hemisphere brain tissue of a donor, deceased at age 69 years, with a diagnosis of Pick's disease - a type of frontotemporal dementia. **a** Lateral view of the hemisphere. **b** Medial view of the hemisphere. **c** Custom, subject-specific 3D printed mold created using a segmentation of the MRI scan. **d** Hemisphere fits seamlessly inside the mold and is ready to be slabbed. **e** The notches in the mold guide the knife to ensure uniformly parallel and equidistant cuts of the tissue. **f** Hemisphere inside the mold after the slabbing is complete

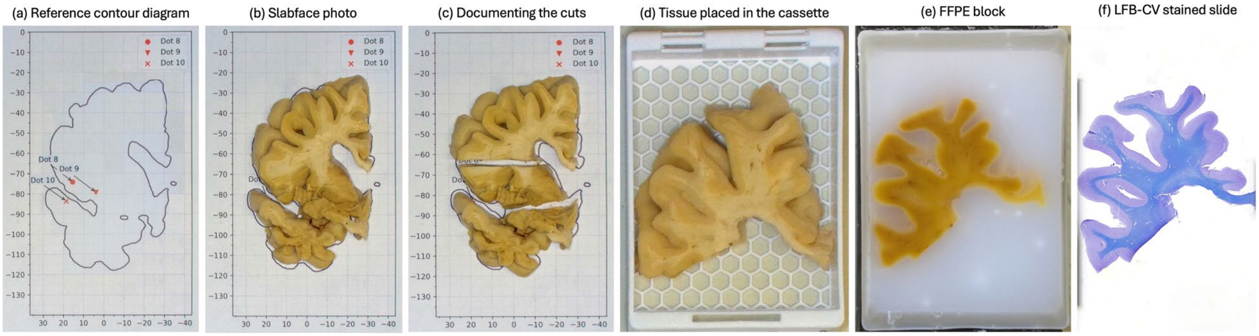
(a) Reference contour diagram

(b) Slabface photo

(c) Documenting the cuts

(d) Tissue placed in the cassette

(e) FFPE block

(f) LFB-CV stained slide

Fig. 5 Histological tissue processing. **a** Reference diagram shows an approximate outline of the tissue for a given slab. The cortical landmark positions are marked using the red markers. The figure shows inferior frontal gyrus (dot 8), insula (dot 9), and the ventrolateral part of the inferior temporal gyrus (dot 10). **b** 1 cm slab of hemisphere tissue placed on the reference outline. **c** If a slab is too big to fit in the 2×3 inch cassette, it is further cut into two or three segments. Cuts are made while keeping the dots in mind and documented for aligning the tissue during registration. **d** The superior segment of the tissue placed in the 2×3 inch cassette. **e** Blockface photo of the paraffin embedded block mounted on the microtome (microtome not pictured). **f** Digital scan of an LFB-CV stained 30 μm thick slide

Brain slabbing: For cases with a diagnosis of AD or LBD, the medial temporal lobe (MTL) was dissected from the hemisphere and then scanned in a 9.4T MRI scanner, slabbed using a MTL-specific 3D printed mold, and underwent serial histological sectioning that enables three-dimensional mapping of pathology. The MTL processing and analysis is described in [16, 44]. The remaining tissue in the hemisphere was processed in a manner similar to the other whole hemisphere specimens. The notches in the 3D mold were used to guide the knife during cutting of the hemisphere. Figure 5 shows the following details of processing a tissue slab. The slabs were cut into segments that fit in 2×3 inch biopsy cassettes and placed with the anterior side facing downwards and immersed in 10% neutral buffered formalin. Whole coronal slabs in the first and last third of the brain usually fit within the dimension of a single cassette. Larger slabs in the middle of the brain were further cut into two (superior and inferior) or three (superior, middle, and inferior) parts to ensure optimal fit in the cassettes. The cuts were made while keeping in mind the position of the dots marking the regions of interest and each cut was documented on the printout with the tissue outline to help with manual initialization for registration later. More recently, we also started documenting pictures of the anterior face of the cut slab with an overhead mounted camera set up with the result as shown in Fig. 5c. Cassettes were labeled with the INDD ID (anonymized ID assigned to each autopsy patient in the Integrated Neurodegenerative Disease Database), slab number, segment (superior, middle, or inferior, if applicable), and an asterisk if the slab contained a region of interest.

Tissue processing: The tissue slab cassettes were processed at the Pathology Core Laboratory within the Children's Hospital of Philadelphia Research Institute and the CNDR at the University of Pennsylvania. A 54-h program was followed using the Thermo Scientific Shandon Excelsior ES tissue processor to get paraffin embedded slabs. This included a 60-minute formalin fixation step to preserve the cut tissue structure and prevent degradation. Next, the tissue was dehydrated to remove any water and prepare it for embedding. To avoid any tissue distortion, this was done gradually by immersing the tissue in six increasing concentrations of ethanol for increasing durations (70% for 2 h, 80% for 3 h, 90% for 3 h, 95% for 4 h, 100% for 5 h, and 100% for 5 h). The dehydrated tissue was then processed with xylene as a clearing agent three times - 4 h, then another 4 h, and lastly 6 h. This step removed all the ethanol and the removal is essential for the paraffin to embed in the tissue correctly. The above steps were all carried out at room temperature. The wax infiltration, which requires the paraffin to be liquid, was done at 64° C. The infiltration sequence included waxes with increasing melting points and processing for 5 h, then 6 h, and another 6 h to ensure complete infiltration. After this, we embedded the samples in paraffin using stainless steel molds.

Tissue sectioning: The paraffin-embedded blocks were processed at the Penn Digital Neuropathology Lab (PDNL). A deionized water bath was prepared and set to 42° C. A 25% glycerol tray was floated on the water bath to be used as a softening agent. Blocks were mounted on a sliding microtome and paraffin sections were defaced until the full tissue cross-section of each block was fully exposed. The block face was then soaked in the 25% glycerol to soften the wax and excess liquid was carefully removed using KimWipes. The block was remounted on the microtome and 30 μm-thick sections were cut and floated on the water bath. Before cutting each section, we took a blockface photograph of the paraffin-embedded slab with an overhead mounted camera as shown in Fig. 5e. Charged microscope slides (Histobond® + Supa Mega Slides, catalog number 71881-60) pre-labeled with the corresponding INDD ID, slab number, and segment were used to pick up the tissue sections. We generally created 5 to 6 slides from consecutive sections per block to ensure continuity and be used for various histological and immunohistochemical staining. Tissue slides were left to air dry for 2–3 h and then placed in the oven overnight at 60° C. The remaining paraffin-embedded tissue block is stable can be stored at room temperature for any future use.

Histological staining and immunohistochemistry: We used two routine histological stains (1) LFB-CV - Luxol Fast Blue (0.1% in 95% alcohol; Electron Microscopy Sciences, catalog number 26056-15) counterstained with Cresyl Violet (Sigma-Aldrich, catalog number C0775) and (2) H&E - Hematoxylin & Eosin (Fisher Scientific, catalog number 6765001) which provide a good visualization of the cytoarchitecture. Additionally, we used different immunohistochemical (IHC) stains based on each project's requirements. Specifically for this study, we used the AT-8 antibody (Thermo Fisher Scientific, catalog number MN1020) for phosphorylated tau.

Digitization: Slides were then scanned using a TissueScope LE120 scanner (Huron Digital Pathology; St. Jacobs, Ontario, Canada) at 0.4×0.4 μm^2 resolution, 20× magnification. Each scanner tray has 6 tray slots and the scanner can hold 10 trays. The total scanning time for a full set of slides was 6 h. Information such as date, type of staining, and antibody concentration was documented in a Huron database and barcodes linking the information to corresponding slide were attached to each slide. The images were also uploaded to PHAS[2] which allowed for easy visualization and annotation of large-scale histology databases via a web browser. The annotation feature was used to mark sampling regions for quantitative pathology analysis and creating labeled training data for deep learning networks as described in later sections.

---

[2] https://github.com/pyushkevich/histoannot.

MRI to histology registration to obtain cortical landmark locations on IHC slides

After obtaining the hemisphere MRI and requisite histological data, we used the following computational pipeline to register the MRI to histology. We use open-source medical image processing packages Convert3D[3] and greedy[4] for the registration. The aim of the registration process is to obtain the exact region on the IHC slide that corresponds to the cortical landmark in the MRI. The AT-8 IHC antibody marks tau pathology, primarily observed in the cortex, but it is not a direct metric to segregate white matter (WM) and gray matter (GM). In case of no pathology, it does not show any contrast between the GM and WM as seen in Fig. 7c. This makes it very hard to perform registration between MRI and the AT-8 stained slide directly. Instead, we opted to reconstruct both the MRI scan and the IHC slide in a common reference space of a cytoarchitectural histology slide such as H&E or LFB-CV which more clearly define GM-WM boundaries. These stains show the most contrast between the white matter and gray matter regions, as seen in Fig. 7a, and hence provide better features to match with the MRI scan during registration. We first registered the MRI to the reference histology slide and then also registered the IHC slide to the same reference histology slide. Once in this common space, the segmentation containing the cortical landmark, when overlaid on the IHC slide, mapped the dots from MRI space to the IHC slide.

MRI to reference histology registration: The 3D printed mold-guided slabbing and the cortical landmark labels gave us an approximate reference location for the histology slide in the hemisphere scan. We used these virtual slabs shown in Fig. 2h to obtain a 1 cm thick region of the MRI corresponding to tissue slab of the reference histology slide. We initialized the registration with this smaller MRI region instead of the entire hemisphere. Each landmark label in the original hemisphere segmentation was a 3×3×3 dot. To account for the out of plane deformations during the registration process, we dilated each labeled dot throughout the coronal plane in the 1 cm thick slab segmentation. We used simple thresholding and random forest classifier to obtain a tissue mask from the reference histology slide. The mask was used to define the boundaries for registering the tissue.

First, the MRI slab was rotated and translated into the space of the reference slide based only on the image centers. An ITK-SNAP workspace was created with this initial alignment of the two images and we used the manual registration tool from ITK-SNAP to refine this alignment. We set the skew ratios of all axes to 1.1 to account for tissue shrinkage during histological processing. Next, we aligned the MRI coronal plane to best fit the reference tissue. This best alignment was used as the starting point for the following automatic registration steps.

All automatic registration steps were performed sequentially in a coarse-to-fine fashion. The manual alignment was used to initialize rigid registration, the rigidly registered image used to initialize affine registration, and finally affine registered image was used to initialize deformable registration. The number of iterations for multi-resolution schedule was derived empirically by running a few test cases and comparing registration results. As seen in Fig. 6, the reference histology slide, and the MRI are quite disparate in appearance. To close this gap, we used a simple strategy of only using a single channel from the RGB histology slide image (empirically, green channel in case of LFB-CV or H&E) to create an "MRI-like" image for registration purposes. This transformation allowed us to use the weighted normalized cross-correlation metric which better accounts for non-overlapping regions between the fixed and moving images during registration. There are other, more complex strategies like using MIND (modality independent neighborhood descriptors) [45], color deconvolution [46], or contrastive learning [47] for better image representation. But we found that using a single channel from RGB histology image in lieu of the original image was sufficient for our use case. Some results using this pipeline are shown in Fig. 6.

(See figure on next page.)

Fig. 6 MRI to reference histology registration. **a** The coronal plane of the MRI scan with the regions of interest marked with the colored dots (boxes shown for emphasis). The white line denotes the cut in the tissue made during the slabbing process. See Fig. 5c for reference. **b** The reference histology slides roughly aligned with the MRI scan. Top photo is the original RGB reference histology slide. We used either the H&E or LFB-CV stain as the reference slide. We used a single channel (green) from the RGB image to mimic an "MRI-like" appearance of the histology slides. The MRI slab was registered to this single-channel image. **c** Reference histology slide overlaid on the registered MRI. After succesful registration, we get the corresponding regions of interest on the histology slide

---

[3] https://github.com/pyushkevich/c3d.

[4] https://github.com/pyushkevich/greedy.

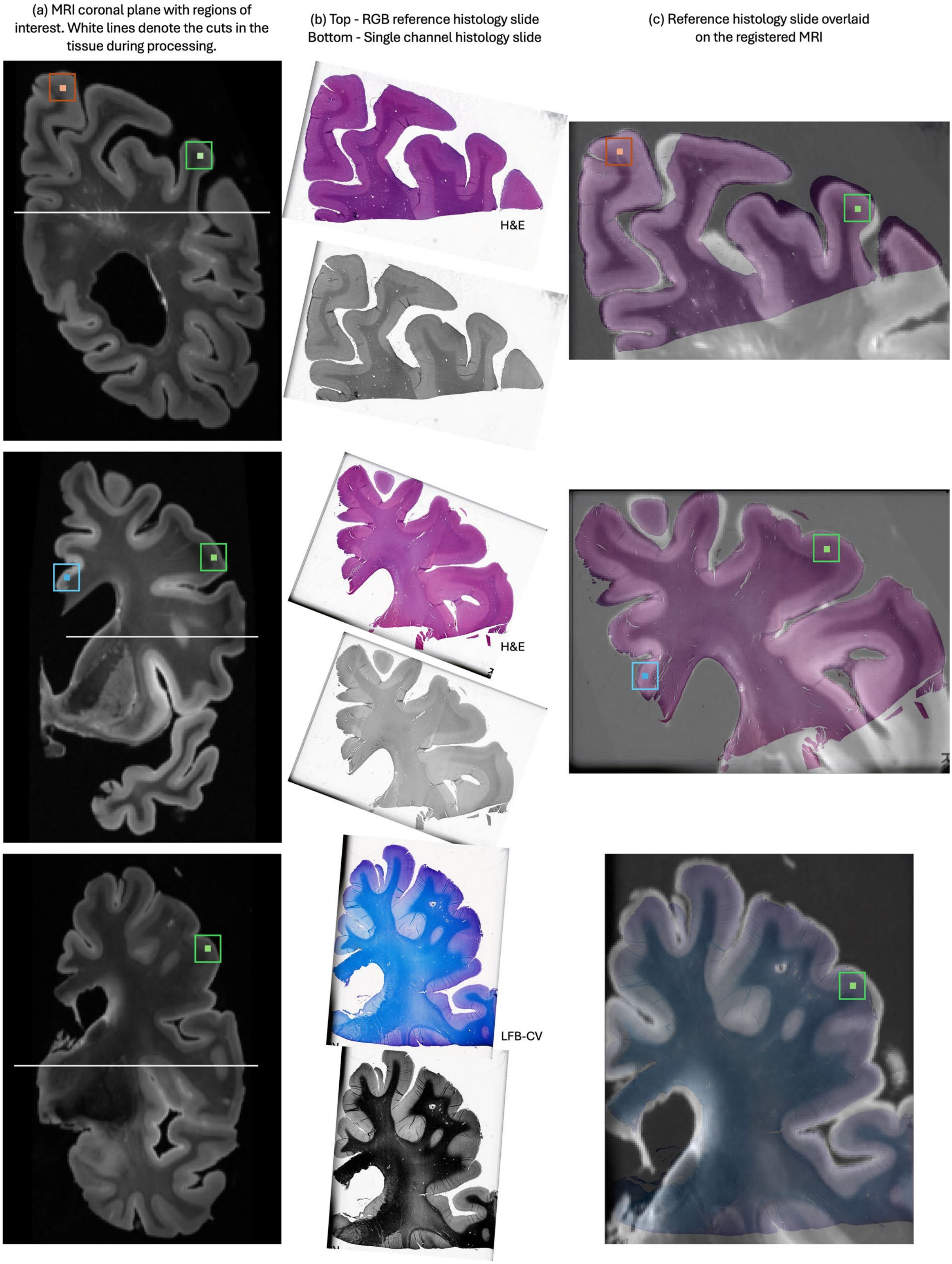

Fig. 6 (See legend on previous page.)

We manually validated the results of the registration pipeline. We saved registration outputs after every stage (manual alignment, rigid, affine, and deformable registration) of the MRI to reference histology registration pipeline. For this, we used a contour tracing strategy used and validated in [16, 34]. We generated the contours for the reference histology image and overlaid the contours in red on all the output images. We visually compared these images laid side-by-side to decide the best result. The best resulting transform was applied to the segmentation containing the dot label for the cortical landmark. Examples for this validation scheme are included in supplementary figure 2.

IHC to reference histology slide registration: This was a fully automated registration process similar to the coarse-to-fine scheme used for MRI to reference histology registration. A piecewise registration approach made this step more robust to the frequent tearing, folding, or shearing of tissue that can occur during slicing histology slides. It ensured that any local deformities in the slides were confined to a single region and did not affect the entire registration. We partitioned the binary tissue segmentation, obtained in the previous step, using image-graph-cut[5] an open-source utility that applies the METIS graph partition algorithm [48], as shown in Fig. 7b. The number of chunks were decided based on the area of the segmented tissue while ensuring each chunk is at least 10% of the total foreground. Each individual piece in the multi-chunk segmentation mask was used as the region of registration and registered independently of each other. A regularization term was used to penalize the overlap between the various separate chunks of the mask.

Both the slides were first converted to grayscale. We initially performed global rigid registration that only accounted for the image centers. Next, we performed piecewise rigid registration on the globally registered images and lastly, performed piecewise deformable registration. We again used the weighted normalized cross-correlation metric for all registration steps. We validated the results of the registration using the same contour tracing approach. The results of the registration, along with the validation contours, are shown in Fig. 7.

Cortical landmark regions on the IHC slide: As the final step, to get the region of interest on the IHC slide, we used the slab segmentation containing the labels obtained after the manual validation of the MRI to histology registration. We overlaid this segmentation on the registered IHC slide which gave us the location of the cortical landmark in the IHC space. The locations of the cortical landmarks were uploaded to our histology annotation server. Using these locations as a guide, we marked up to 5 patches in the same and/or neighboring gyri (to avoid sampling bias) which would be used for quantitative pathology measurements as shown in Fig. 9B, a. All the sampled patches only included the GM cortex tissue.

Quantitative measures of pathology using weakly supervised learning

We used Wildcat [49], a weakly supervised deep learning based approach for classifying neuronal tangles and threads in the AT-8 IHC slides. This method has been previously trained and validated for measurements of neurofibrillary tangle burden [16, 44], and phosphorylated tau and TDP-43 pathology [14] in the MTL. Wildcat architecture is based on the ResNet-101 but we replaced the last fully-connected layer with a class pooling and a spatial pooling layer. This provided a convenient way to get pointwise object localization and visualize the heat maps for multiple classes. We modified the Wildcat architecture with a U-Net like structure by adding upsampling layers with skip connections [50] to generate higher resolution heat maps - our heat maps are 1/2 the input image size versus the original architecture's 1/16 original size. We used the bounding boxes we placed on the AT-8 slides after registration to sample patches of the histology slide for inference as shown in Fig. 9B. We integrated over the heat map for each class to obtain a quantitative score of pathology for that region.

Labeled training data generation: We trained users of various levels of training (post-docs, doctoral students, and pre-doctoral researchers) on key morphological features of tau inclusions across ADRD in a series of group meetings using whole-slide images (WSI) of digital histology images of AT-8 stained tissue sections. After a

(See figure on next page.)

Fig. 7 IHC to reference histology registration. **a** Reference slide (either H&E or LFB-CV stain) with its contours traced in red. The contours are obtained using Canny edge detection and used as a reference to visually assess the quality of registration. **b** Tissue segmentation mask divided into parts using the METIS graph partitioning algorithm. Each part is registered separately and there is a regularization term to reduce overlap of the individual parts. **c** IHC slide (AT-8 antibody) after registration. The red contours are the same as (**a**) obtained from the reference slide and are overlaid on the IHC slide. We see good registration performance even in cases with less than ideal tissue e.g. row 2

---

[5] https://github.com/pyushkevich/image-graph-cut.

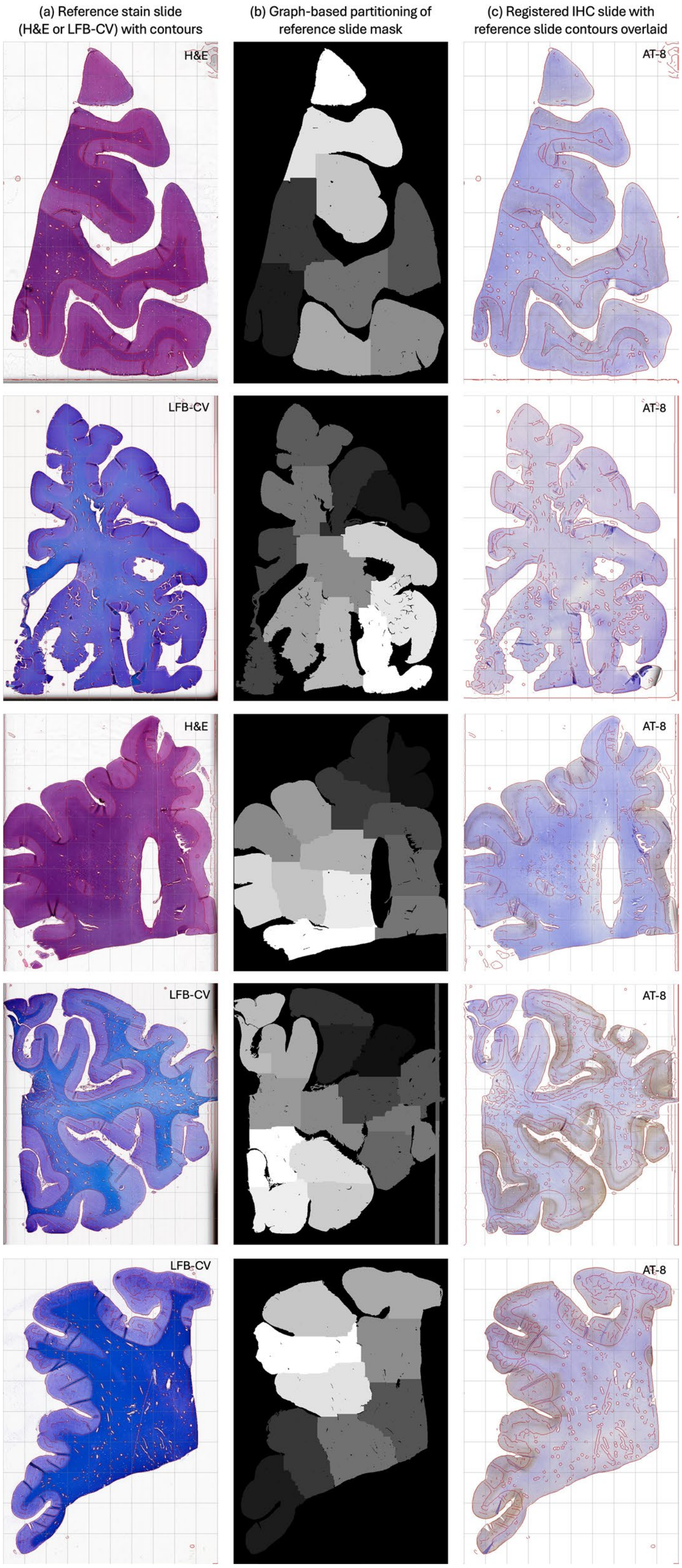

Fig. 7 (See legend on previous page.)

series of real-time training sessions led by expert reviewers (E.B.L., D.J.I., D.T.O., P.A.Y.) trainees annotated example patches from a random series of WSI on their own time using the online PHAS tool which keeps a visual record of exemplar patches which were reviewed for accuracy by expert raters. This process resulted in 70,000 examples of tangle-like objects (tangles, pre-tangles, Pick bodies, and ballooned neurons), threads (tau threads, neuritic plaques, tangle-associated neuritic cluster, tau grains, and tau threads in white matter axons) and background (healthy neurons, normal-appearing tissue, artifacts, dirt, etc.) classes across 261 AT-8 IHC slides from 139 autopsied brains, that were used for training our classifier. A patch of size 512×512 was extracted from around the labeled boxes. Note that, we only used 4000 samples of each class for training so labeling 70,000 examples was probably more than necessary.

The training data was labeled on slides sectioned from the diagnostic sampling hemisphere and their processing slightly differed from our whole hemisphere IHC slides. The training data slides were 20 μm thick and were scanned using Aperio ScanScope digital scanner (Leica Biosystems; Nussloch, Germany) at 0.5×0.5 μm^2 resolution as compared to our slides with 30 μm thickness and scanned with TissueScope LE120 at 0.4 μm^2 resolution. However, the IHC staining was done in the same way and their visual appearance was similar enough for the model to show comparable performance on both the data.

Training and validation: We trained the model using 5 fold cross-validation - we randomly divided the 139 specimens into mutually exclusive training (111 specimens) and test (28 specimens) set. The model was trained on 4000 samples of tangles, threads, and background class and these samples came only from the 111 specimens in the training set. We also used a validation set of 400 samples per class to determine training progress and early stopping criteria to prevent the model from overfitting. The model was tested on patches from the 28 specimens in the test data. We repeated this process 5 times by randomly generating the training and test splits and picked the model with the highest test accuracy among them. The chosen model could classify tangles with 96.32% ± 1.1% (95% CI) accuracy and threads with 95.74% ± 0.57% (95% CI) accuracy.

Generation of pathology burden maps: We applied the trained Wildcat model on the sampled regions from the IHC slides. The class activation maps were extracted from the class pooling layer and thresholded at zero. To get a cumulative, quantitative measure of pathology, we tried various methods of aggregating the image level statistics. This included taking the mean, median, and various percentiles. Since our sampling here is optimized to match specific GM cortex on MRI, we have a relatively focused region of interest for digital histology. Thus, lower quantiles did not accurately capture the full pathological burden in the given region. We performed a detailed analysis using different summary measures (mean, median, maximum, 25th, 75th, 90th, 95th, and 99th quantiles) in our previous work [14] and based on that chose to use to 99th quantile of intensity values as a quantitative measure of pathology.

Measuring cortical thickness at landmarks

We used the previously labeled cortical landmarks in the whole hemisphere segmentation. All steps in this process are illustrated in Fig. 8. A small isotropic neighborhood of the surrounding gray matter of these cortical landmarks was semi-automatically segmented in ITK-SNAP using the active contour segmentation [43, 51]. A 3D segmentation was obtained from this regional segmentation and we created a “skeleton” of this 3D shape using Voronoi skeletanization [52]. This technique uses Voronoi diagrams, which partition a space based on distances to a specific set of points, to derive the central structure (skeleton) or medial axis of a shape. This medial axis is a reduced, simplified surface representation that maintains the topology and general layout of the original shape. The skeleton captures the connectivity and main form without excess details. For a 3D shape, the skeleton points are centers of the biggest sphere that can completely fit inside the shape (maximally inscribed) at that point. The diameter of the sphere gives us the local thickness of the structure (Fig. 9). We used this Voronoi skeletanization to compute the cortical thickness measurements at anatomical landmarks in the hemisphere. This approach has been previously used and validated in [28, 53].

Point-wise cortical thickness and regional pathology associations

To assess the localized atrophy patterns, we performed point-wise surface-based thickness analyses in the fsaverage [54, 55] template space. In particular, we fit a generalized linear model (GLM) via threshold-free cluster enhancement (TFCE) [56] with cortical thickness (mm) as the dependent variable, and pathology measurement from a single region (e.g. anterior cingulate in Fig. 10a) as the dependent variable; age, sex, and postmortem interval (PMI) were the covariates. The models were corrected for multiple comparisons ($p<0.1$) using family-wise error rate (FWER) [57] and permutation testing with the Freedman and Lane method (1000 iterations) [58]. Specifically, we used purple-mri[6] developed in [40] to parcellate the whole-hemisphere using the Desikan-Killiany-Tourville

---

[6] https://github.com/Pulkit-Khandelwal/purple-mri.

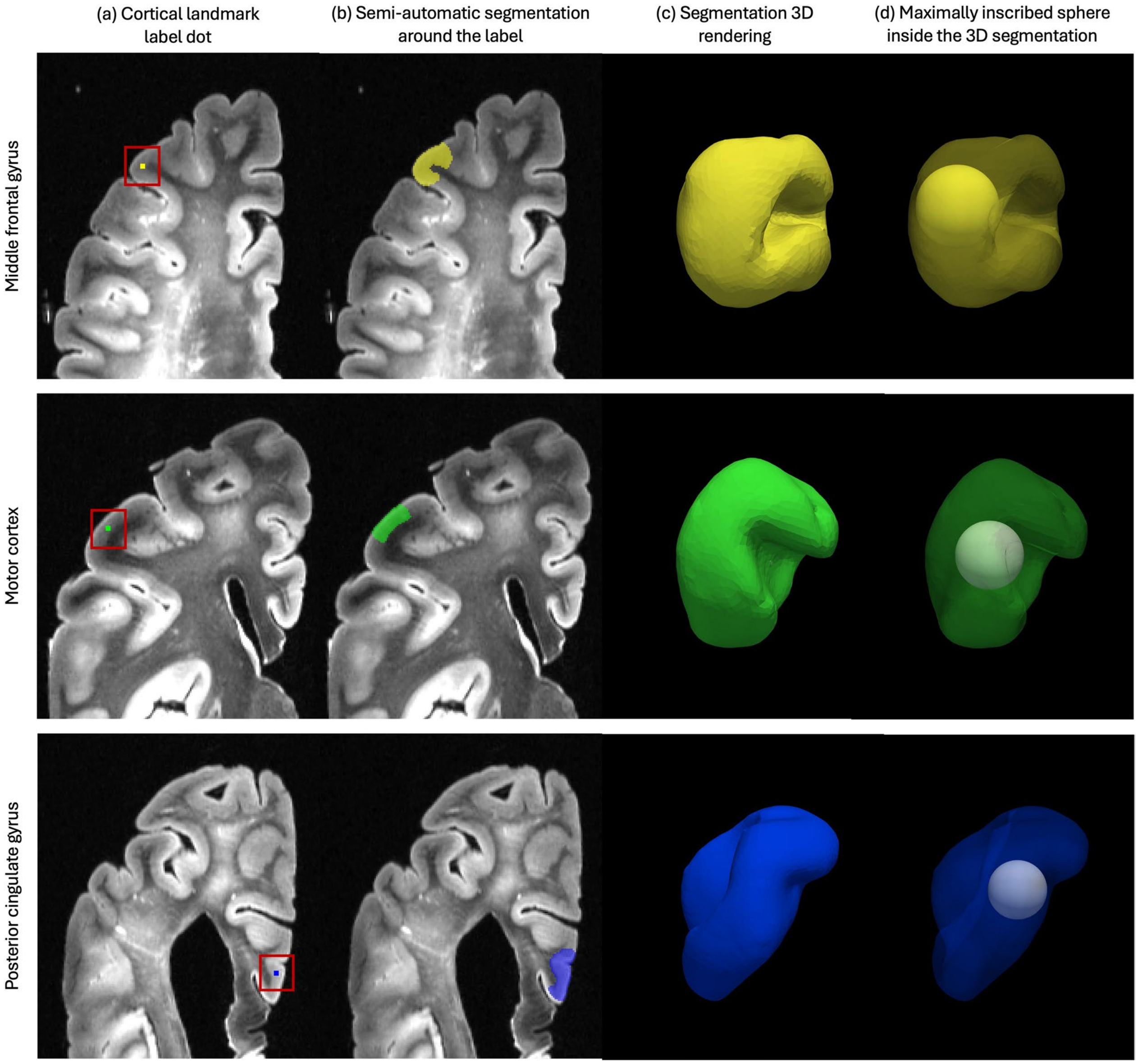

Fig. 8 Cortical thickness measurement. Cortical thickness at anatomical landmarks was measured as the diameter of the maximally inscribed sphere using Voronoi skeletanization. Figure shows the process for three areas - middle frontal gyrus, motor cortex, and the posterior cingulate gyrus. **a** Cortical landmark labeled as a 3×3×3 voxel dot in the whole hemisphere segmentation. **b** An isotropic region around the dot label is semi-automatically segmented in ITK-SNAP using the active contour segmentation. **c** 3D rendering of the segmented region. **d** Maximally inscribed sphere after Voronoi skeletanization inside the 3D rendering. The diameter of this sphere is used as the cortical thickness measurement for this anatomical landmark

(DKT) altas and then computed whole-hemisphere cortical thickness using FreeSurfer v7.4.0 [55]. Thickness map of each individual subject was then warped to fsaverage template space and smoothed with a Gaussian kernel of full-width half maximum (FWHM) of 5 mm. In our analyses all the left hemisphere surfaces were flipped to match the orientation of the right. The t-statistic map and the p-value (alpha<0.05; uncorrected) for the pathology measurement was visualized in the fsaverage template space.

Association of p-tau with regional cortical thickness

Prior postmortem MRI studies found widespread patterns of association between tau pathology in the MTL and structural measures, including hippocampus and amygdala volumes [59], MTL [13, 60], and whole-hemisphere cortical thickness [40]. However, the relationships between tau accumulation in areas outside of the MTL and cortical thickness in corresponding anatomical locations in the ipsilateral hemisphere has not been extensively studied [61]. Previous studies have linked tau accumulation with neuronal loss and subsequent tissue atrophy which suggests that increased tau pathology in a region should be associated with decreased cortical thickness [62–64]. Using our pipeline for MRI-guided histology and quantitative measurements of pathology and cortical thickness, we present a preliminary analysis comparing quantitative phosphorylated tau (p-tau) score with linked ipsilateral, whole hemisphere ex vivo morphometry. This study examined hemispheres from 29 brain donors (14 female, 15 male) autopsied between 2018 and 2021, with an average age of 78.83 years (range 63-99) at death and an average postmortem interval of 20.22 h (range 4-58). All the brains had a primary or secondary neuropathological diagnosis of AD or primary age-related tauopathy (PART), without evidence of other tauopathies or frontotemporal lobar degeneration involving TDP-43 inclusions. The demographics and neuropathological breakdown of the cohort is presented in Table 1. All the hemispheres followed the scanning, fixation, and histological processing described above. Since the MTL is excised for 9.4T MRI in AD and PART brain donors at our center, most hemispheres did not have an intact MTL. This also meant that we did not have enough data points for superior temporal gyrus, inferior temporal gyrus, insular gyrus, entorhinal cortex, Broadmann Area 35, Cornu Ammonis 1, subiculum, and parahippocampal cortex. The characterization of tau pathology in these regions in the MTL is presented in [44].

We performed all analysis in Python using open-source libraries scipy (version 1.12.0), statsmodels (version 0.14.0), and pingouin (version 0.5.5). We only used regions of interest that had 15 or more measurements available. We calculated one-sided partial Spearman rank-order correlation coefficient to assess the correlation between cortical thickness and pathology with age, sex, and postmortem interval (PMI) as covariates. The results are reported in Table 2. We also separately calculated the one-sided Spearman correlation coefficient without any covariates; and using only sex and PMI as covariates (supplementary table 1).

Results

Partial Spearman correlations between cortical thickness and tau tangle with age, sex, and PMI as covariates were significant in the middle frontal gyrus ($r = -0.3961$, p-value $= 0.0419$; $n = 23$). Partial Spearman correlations between cortical thickness and neuronal threads with age, sex, and PMI as covariates were significant in the posterior cingulate gyrus ($r = -0.4612$, p-value $= 0.0270$; $n = 21$), anterior cingulate gyrus ($r = -0.4812$, p-value $= 0.0216$; $n = 21$), and the middle frontal gyrus ($r = -0.4077$, 0.0372; $n = 23$). We also report the results with no covariates and only sex, PMI as covariates in supplementary table 1.

We also calculated surface-based point-wise correlation between thickness and the regional quantitative neuronal threads measurements in regions where there was significant correlation. The results for anterior cingulate, posterior cingulate, and the middle frontal gyrus (regions marked by the black rectangles) are presented in Fig. 10. The figure shows the t-statistics map on the pial surfaces. We see areas of high t-statistic in all the three regions which is in line with the Spearman correlation coefficients that we obtained previously.

Discussion

In this work, we present a general method to process whole hemispheres for MRI-guided histology in high volume brain banks. It is an end-to-end protocol including scanning the hemispheres, labeling cortical landmarks, generating custom 3D printed molds, slabbing the brain tissue, histological processing, and staining. The FFPE blocks of the whole hemisphere created during the process can be stored indefinitely at room temperature and used in the future to analyze structure-pathology associations in additional anatomical regions, or using new immunohistochemistry techniques. The virtual slabs of the hemisphere and slabface photographs of the tissue provide us a permanent frame of reference with respect to

(See figure on next page.)

Fig. 9 Wildcat activation maps. **A** Sample patch-level activation maps of neuropathology. Each column shows a sample patch of tissue and the class activation maps for the patch for each class. The model produces highest activation (seen as bright spots) for areas where it detects an example of that particular class in the sample. For example, we see bright spots in the tangle class activation map where the model detects tangles in the patch. But there is no activation for tangle class in any area in the other patches. We also see little to no activation for threads and other class for the patch containing the tangle i.e. the model doesn't detect any of these classes in that patch. **B** Wildcat applied to a sample patch of IHC shows how we use Wildcat to get quantitative pathology scores in our pipeline. **a** AT-8 IHC slide of a segment of brain tissue showing the anterior cingulate gyrus in the ROI. The red boxes show the areas of tissues that were sampled to get pathology scores. **b**, **c** Zoomed in views of the patches. **d** Closer look at the sampled patch. The bright rectangular patch was passed to the Wildcat model. **e** Output from the Wildcat model showing the activation map for tau tangles. The bright spots are where the model detected tangles in the patch. **f** Output from the Wildcat model showing the activation map for neuronal threads. The bright spots are where the model detected threads in the patch

(A) Sample patch-level activations of neuropathology

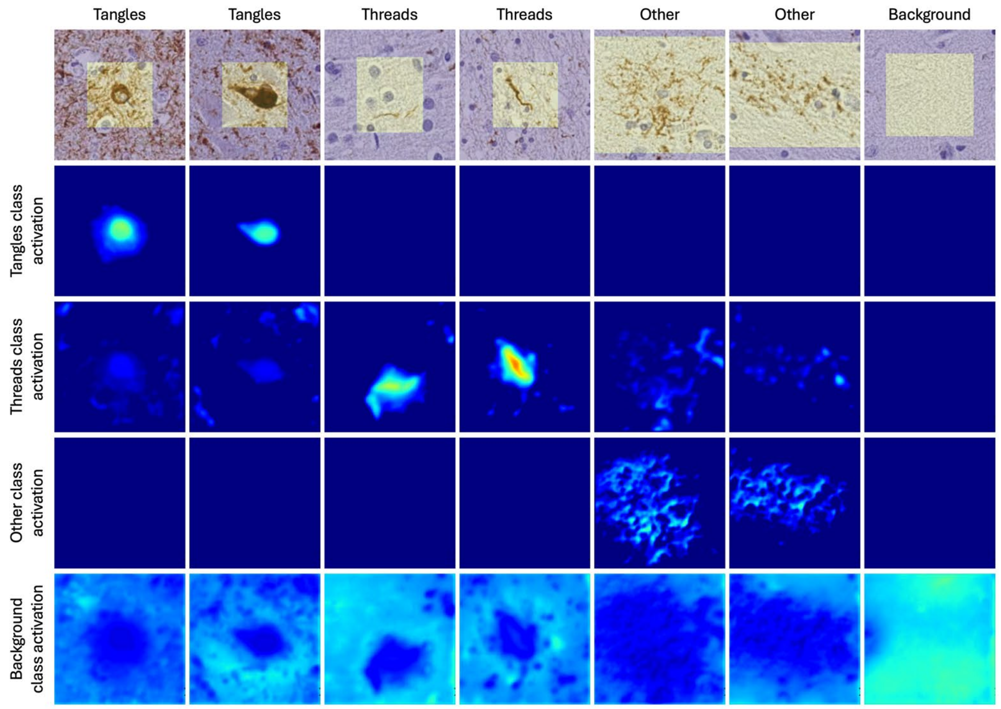

(B) Wildcat applied to a sample patch of IHC slide

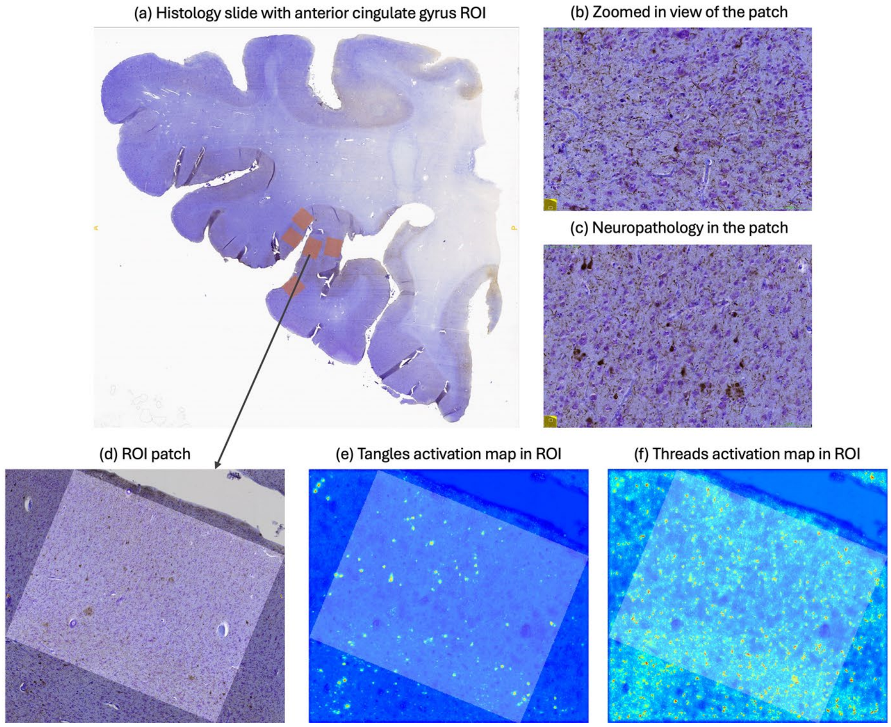

Fig. 9 (See legend on previous page.)

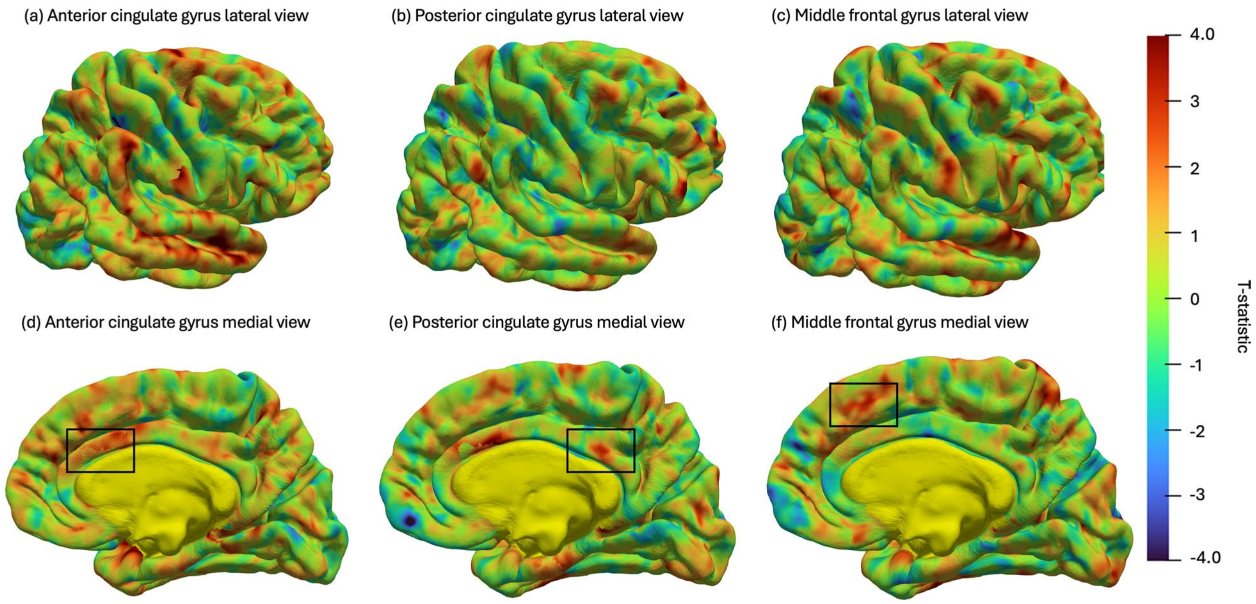

Fig. 10 Template-space point-wise morphometry-pathology correlations. Point-wise correlation between thickness and the regional quantitative neuronal threads measurements in the **a**, **b** anterior cingulate, **b**, **e** posterior cingulate, and **c**, **f** middle frontal gyrus. Generalized linear model (GLM), using threshold-free cluster enhancement (TFCE), was fit to correlate point- wise thickness (mm) with average neuronal threads ratings for each group. The models were covaried for age, sex, and PMI. Shown are the t-statistics maps after multiple comparisons ($p \leq 0.1$) using family-wise error rate (FWER) and permutation testing with the Freedman and Lane method (1000 iterations). The black rectangle in the medial view marks the location of each region in the brain. We see areas of high t-statistic in all the three regions which is in line with the Spearman correlation coefficients that we obtained previously

MRI for these FFPE blocks. We also presented a preliminary computational pipeline to perform MRI to histology registration, obtain quantitative measures of pathology from histology, and cortical thickness measurements from the MRI scans. Beyond enabling spatially-linked morphometry-pathology associations, our postmortem hemisphere processing protocol lays a foundation for improving neuropathological sampling for any future studies. The pipeline will be especially advantageous for studying spatially heterogeneous, "patchy" pathologies – such as cerebrovascular small vessel disease (CSVD), chronic traumatic encephalopathy (CTE), aging-related tau astrogliopathy (ARTAG), argyrophilic grain disease (AGD) – precisely and at a scale that was previously not feasible. The fact that the whole hemisphere is preserved as paraffin-embedded blocks with known spatial correspondence to the ex vivo MRI makes it possible to retrospectively map lesions or regions of interest observed on MRI (either in vivo or ex vivo) to corresponding locations in histology (and vice versa). For example, white matter hyperintensities (WMH) observed on in vivo FLAIR MRI can be investigated histologically, as shown in Fig. 11, by cutting additional sections from the corresponding paraffin block and applying appropriate histological stains. Conversely, the protocol makes it possible to study the spatial distribution of pathologies such as ARTAG and AGD that are "MRI-invisible" but are prominently visible on histology. By mapping the distribution of these pathologies into ex vivo MRI space, and registering ex vivo MRI to a population template [53], it will be possible to characterize the variability in the distribution and spread of these pathologies, perhaps eventually leading to MRI-based biomarkers for their detection. Thus, by providing a scalable method for anatomically informed, MRI-guided sampling, this work paves the way for refining neuropathological diagnostic criteria and sampling protocols to capture both known and novel patterns of regional pathology. Once scaled up, the far-reaching applications of this work could include creating normative and disease phenotype maps of pathology as well as MRI-derived signatures of pathology even applicable to in vivo studies and biomarker development.

Necessity of postmortem imaging: Postmortem whole brain or whole hemisphere MRI scans are not a common procedure in most brain banks that serve AD and FTLD research centers in the United States [65]. However, postmortem MRI is necessary to get the 3D printed mold used in our protocol and establish the one-one reference system between MRI and tissue for histological processing. Antemortem MRI cannot be a substitute for this as fixation-induced deformation and the long interval between antemortem imaging and

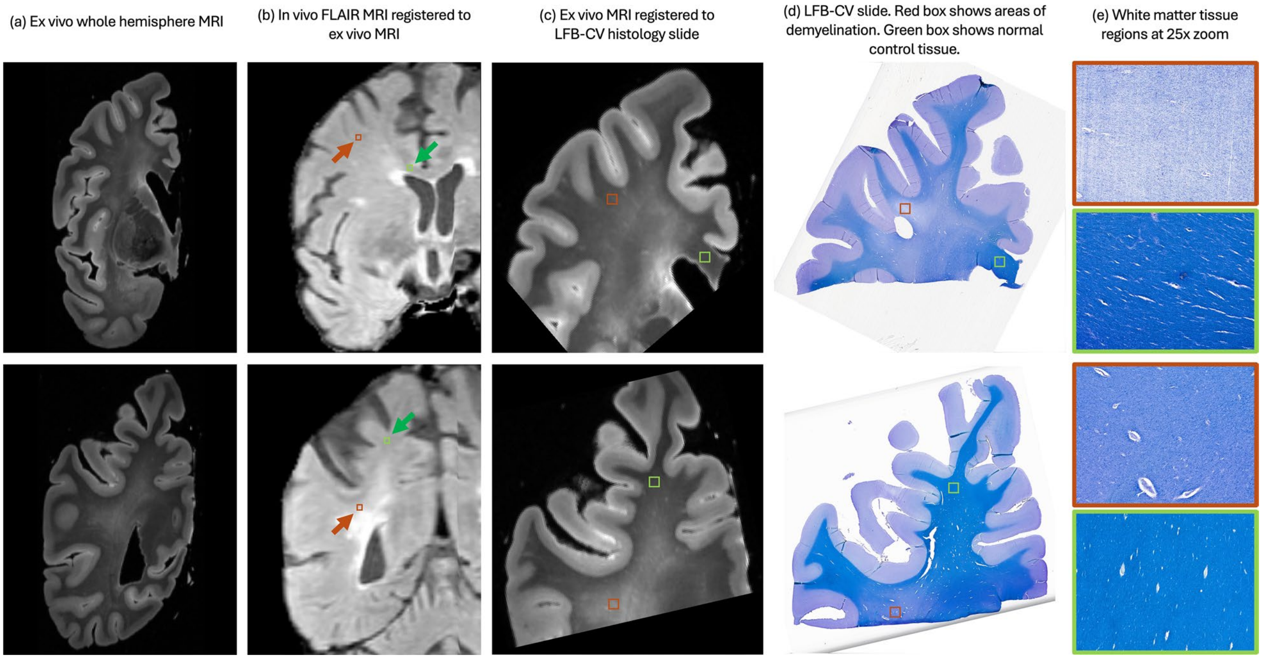

Fig. 11 White matter hyperintensities across modalities. White matter hyperintensities (WMH) are the most prominent MRI markers for vascular pathology. Cerebrovascular pathology (CSVD) is a type of spatially heterogeneous pathology that can greatly benefit from MRI-guided histology sampling. Here we track the locations of WMH across **a** ex vivo whole hemisphere MRI **b** in vivo FLAIR MRI that is registered to the ex vivo MRI **c** ex vivo MRI that is registered to the LFB-CV histology slide and lastly **d** LFB-CV histology slide. LFB-CV (Luxol Fast Blue counterstained with Cresyl Violet) is a stain that enables simultaneous visualization of myelinated fibers and neuronal cell bodies. Myelin appears blue and neurons purple. This dual staining technique enables us to assess both white matter integrity and neuronal density in the brain tissue. In the last column **e** we see the 25x zoomed in tissue regions. Red box shows demyelinated tissue and the green box shows normal control tissue. The regions are marked with boxes on the other modalities as well

time of death result in significant anatomical changes that prevent reliable alignment between antemortem MRI and histological tissue. Among centers that do perform postmortem imaging, there is a great deal of variation in laboratory procedures, and registration between histological images and MRI is rarely the driving factor for tissue processing. Custom 3D printed molds based on the MRI scans have ben successfully used for high volume histological processing in smaller organs such as the prostate [66]. A previous study used brain-specific 3D printed molds for rat and macaque brains [67]. The grooves in the mold were created using species-specific anatomical information from stereotaxic atlases and used to localize the anatomy. [68] have used a custom 3D printed cutting box for cutting whole human brains. A recent pre-print [69] used a reusable container with agar medium for scanning and cutting postmortem brains. However, the set up required a custom-made Tic-Tac-Toe head coil radiofrequency system in the MRI scanner. Agar is also not an ideal medium as it sticks to tissue and cannot be completely removed. Our pipeline improves on these approaches by also including MRI-based patient-specific cortical landmarks and mapping them to the cut sections. This speeds up our downstream registration pipeline compared to the visual matching done in [68]. Our design of the 3D mold also uses less raw material compared to [68] while still having the grooves that ensure parallel cuts.

On the other hand, MRI-guided histology protocols that don't use custom 3D molds have used intermediate modalities such as blockface imaging [19] or MRI scans of the cut brain slabs [15, 70]. Blockface imaging can complement the registration pipeline but cannot do much in case of unevenly cut brain tissue. Re-scanning the cut brain slabs is a delicate, resource-intensive process and also requires the use of a custom container for scanning. [71] have investigated WMH and normal appearing white matter (NAWM) with targeted histopathological sampling using postmortem MRI. However, they did not use any mold and re-scanned each of the coronal slabs of cut tissue in addition to whole hemisphere MRI. As we show in Fig. 11, our protocol can be used to study WMH in a similar manner but without the need for rescanning cut tissue. Our 3D printed mold ensures even cuts and does not require further MRI scanning while also being modular enough to include blockface imaging in the future.

Table 1 (a) Brain donor cohort demographics (b) Primary, secondary, and tertiary postmortem neuropathological diagnoses (c) Global neuropathological stage scores

(a) Brain Donor Cohort							
Number of specimens	29						
Age (mean ± SD)	78.83 ± 9.18 years (range 63–99)						
Sex	14F, 15M						
Hemispheres	14R, 15L						
Postmortem Interval (mean ± SD)	20.22 ± 14.08 hours (range 4–58)						
(b) Neuropathological Diagnoses							
	Primary	Secondary/Tertiary					
Alzheimer's Disease	22	4					
Dementia with Lewy Bodies (DLB)	5	12					
Cerebrovascular Disease (CVD)	1	3					
Primary Age-Related Tauopathy (PART)	1	2					
Limbic-predominant Age-related TDP-43 Encephalopathy (LATE)		10					
Chronic Traumatic Encephalopathy (CTE)		3					
Hippocampal Sclerosis		1					
(c) Global Neuropathological Staging							
Scale	**0**	**1**	**2**	**3**			
Amyloid (A)	3	1	6	19			
Braak (B)	0	5	8	16			
CERAD (C)	5	4	3	17			
Scale	**0**	**1**	**2**	**3**	**4**	**5**	**6**
Braak (6-stage)	0	0	5	4	4	2	14

Our MRI-guided histology sampling protocol is especially valuable for studying spatially heterogeneous pathologies such as DLB, CVD, and CTE which is seen in over half the patients in this cohort

Table 2 Correlation coefficient and p-value for one-sided partial Spearman correlation between quantitative pathology score (neuronal threads and tau tangles pathology) and cortical thickness measurements from the ipsilateral hemisphere with age, sex, and postmortem interval as covariates

Region of Interest (number of data points)	**Correlation coefficient (*p*-value) of one-sided partial Spearman correlation between cortical thickness and quantitative pathology measurements with age, sex, and postmortem interval as covariates**	
	Tau tangles	**Neuronal threads**
Angular gyrus ($n = 18$)	0.0679 (0.5951)	– 0.1346 (0.3162)
Posterior cingulate gyrus ($n = 21$)	– 0.2421 (0.1665)	**– 0.4612 (0.0270)**
Superior parietal lobule ($n = 19$)	– 0.3161 (0.1165)	– 0.4022 (0.0613)
Motor cortex ($n = 24$)	0.4050 (0.9657)	0.2802 (0.8907)
Anterior cingulate gyrus ($n = 21$)	– 0.3988 (0.0506)	**– 0.4812 (0.0216)**
Orbitofrontal gyrus ($n = 19$)	0.2432 (0.8180)	0.2754 (0.8491)
Middle frontal gyrus ($n = 23$)	**– 0.3961 (0.0419)**	**– 0.4077 (0.0372)**
Insular gyrus ($n = 19$)	– 0.0875 (0.3737)	– 0.1712 (0.2631)
Inferior frontal gyrus ($n = 19$)	0.0555 (0.5805)	0.0695 (0.6009)
Primary visual cortex ($n = 15$)	– 0.3936 (0.1028)	– 0.3518 (0.1311)

We report the values for 10 regions of interest in the whole hemisphere. Cortical thickness was measured as the diameter of the maximally inscribed sphere in the MRI segmentation. Quantitative pathology measurements were obtained using a weakly supervised deep learning algorithm. Significant correlations (*p*-value < 0.05) are shown in bold

Other postmortem pathology-morphometry association studies, which do not use any specialized cutting devices, have used in situ MRI [72], regional tissue sample MRI [73–75] whole brain scans [69], and whole hemisphere scans [76–78]. Most studies did not perform any registration between the histology and MRI. Our work also uses higher resolution 7T 0.28 mm^3 isotropic resolution MRI scans compared to the lower resolution 3T 0.6×0.6×1.5 mm^3 MRI scans used in some other large-scale postmortem studies [77, 79]. [74] used a special histological readiofrequency coil to get around it. [73, 75] visually picked the MRI slice that was closest in appearance to the histology slide and then performed nonlinear registration. For quantitative pathology in whole hemispheres, a previous study [80] used high-throughput digital histopathology to algorithmically quantify amyloid and tau tangle pathology in over 600 brain autopsies. However, the study did not include MRI correlates. Our deep learning-based pipeline can also provide more fine-grained quantification of heterogeneous pathology in digital slides as compared to some of these methods.

A previous work from our group studied the association of phosphorylated tau pathology with whole-hemisphere ex vivo morphometry [28]. However, the work used semi-quantitative pathology ratings from the contralateral hemisphere as measures of pathology. Another limitation of the study was the unavailability of exact homologues for pathology-thickness measurements. Out of the 16 regions used for the study, only seven regions had paired thickness and histopathology scores. For the remaining nine “exploratory” regions, pathology measurements from proximal regions were used for the analysis. Compared to these proximal regions, our model showed significant correlation in the anterior and posterior cingulate gyrus, and middle frontal gyrus. Our study also suffered from a lack of measurements from the MTL region where these associations are observed most strongly. Despite this, the stronger correlations in the paired regions demonstrate the utility and importance of studying ipsilateral, quantitative morphometry-pathology association in postmortem tissue.

Limitations and caveats: There are a few shortcomings in our current MRI to histology registration workflow. The downside of using 75×50 mm slides for histology, compared to the more widely used 75×25 mm slides, creates more distortions like shearing, tearing, folding, and staining artifacts. We have also optimized our microtome sectioning to now create sections of 20 μm thickness which has reduced folding of the tissue when mounting on the slides. Due to the nature of our research center and brain bank, we mostly deal with diseased brains with varying degrees of atrophy. This also means compromised tissue integrity which makes it harder to perform consistent histological processing. We assume that the tissue has been cut parallel to the coronal MRI acquisition plane; which is a fair assumption given our use of the custom 3D molds for guiding the cuts. However, in reality, there may be out-of-plane distortions either during the initial cutting of the tissue or sectioning of the FFPE block on the microtome. In an optimization-based deformable registration, we need to strike the right balance with regularization to model these out-of-plane deformations. In our future work, we plan to use the slabface (images of the cut tissue taken before paraffin embedding, see Fig. 5b) and blockface (images of the FFPE block mounted on the microtome, see Fig. 5e) photographs as intermediate modalities in the registration workflow.

Our initial SOP for labeling cortical landmarks did not take into consideration the depth of the labels from the anterior face of the slab in which they were located.

During manual evaluation of the registration results, we realized that in some cases, the cortical landmark was localized to a particular coronal plane that was further posterior than the histology section. To prevent such cases, we updated our labeling SOP to ensure that the labels were placed within 2 mm of the anterior face of the 1 cm thick slab. In some other cases, the histology tissue for the region of interest was too distorted to be processed for quantitative pathology measurements. As we have processed more cases, the frequency of such tissue distortions has greatly reduced. But a workaround for such cases can be to use a "histology-first" approach to labeling regions of interest. We would use the MRI labels to localize the slabs to be processed, but specify the region of interest on the histology slide first. After registration, the cortical thickness measurements will be taken from the corresponding region on the MRI.

Finally, it's important to note that our postmortem imaging studies project commenced shortly before the onset of the COVID-19 pandemic, and this cohort included specimens with higher fixation period which significantly affected tissue quality. Previous works have shown that paired helical filament (PHF) tau can undergo dephosphorylation over longer fixation times [81, 82], however, the anatomical distribution of the pathology is still preserved. We have also observed significant shrinkage in the tissue volume for the brains that have been in fixation for a long duration. In the more recent autopsies at our center, we have implemented a standardized 60-day formalin fixation period. As with other limitations, we anticipate that greater consistency in formalin fixation would likely strengthen the observed associations between structure and pathology. Another factor to be considered is the postmortem interval, which is the period from time of death to autopsy, and can affect tissue integrity and protein markers. A previous work has shown no detectable protein loss for a PMI of up to 22 h [83] and another work shows positive staining for all proteins for a PMI of up to 3 days [84]. Our mean PMI of 20.22 h is well within these estimates for postmortem tissue analysis. Furthermore, as suggested in these studies, we have used the postmortem interval as a covariate in all our statistical analysis to account for the effect of varying PMI.

Future work: We want to create a high-throughput pipeline for MRI-guided histology processing in high volume brain banks. Our goal is to reliably automate all image processing and computational steps following the digitization of histology slides using a range of histopathological stains for various features of neurodegeneration in adjacent slides. We recently developed and validated a surface-based, whole hemisphere parcellation scheme to perform point-wise morphometry analysis in native subject space for ex vivo hemispheres. We plan to use this pipeline to automate the labeling of the cortical landmarks for MRI-guided histology and obtain more accurate cortical thickness measurements. Our current registration pipeline involves a manual initialization step for the subsequent automatic registration. By incorporating intermediate modalities like slabface and blockface photographs, we hope to have an end-to-end automated registration pipeline. We also plan to train and validate our WSL quantitative pathology model for α-synuclein and TDP-43 pathologies in whole hemisphere histology. These are the two most frequently occurring co-pathologies in AD patients. It is important to have a measure of all the co-pathologies to get the most accurate morphometry-pathology associations in ADRD.

Conclusions

In this study, we present a standardized protocol for operationalizing postmortem pathology-MRI association studies in Alzheimer's Disease and related disorders through MRI-guided histology sampling. We use ultra-high resolution 7T ex vivo MRI scans to guide the histological sampling of brain tissue. This method overcomes the limitations of traditional brain banking practices, which often rely on limited and sparse regional sampling. Our approach leverages patient-specific 3D printed molds obtained from ex vivo MRI scans which allows precise and reproducible histological sampling while maintaining a permanent spatial frame of reference.

Furthermore, we developed a semi-automated MRI to histology registration pipeline, which aligns histology and IHC slides to corresponding MRI coronal planes facilitating correlation studies between imaging features and neuropathological findings. We use a weakly supervised deep learning-based architecture to calculate quantitative measures of pathology, which allows for objective and scalable analysis of pathology. We apply this to analyze a cohort of 29 postmortem brains with ADRD neuropathological diagnosis and demonstrate correlation between cortical thickness and phosphorylated tau pathology, thus validating our protocol for studying spatially-linked quantitative morphometry-pathology associations in postmortem whole hemisphere brains.

This work not only establishes a high-throughput and reproducible framework for MRI-guided histological sampling but also lays the foundation for future studies aimed at developing more accurate in vivo biomarkers for neurodegenerative diseases such as creating normative and disease phenotype maps of pathology and studying MRI-derived signatures of pathology. The flexibility of our protocol allows for its adaptation to other neuropathologies such as TDP-43 and α-synuclein, thereby expanding its applicability to a broader spectrum of neurodegenerative conditions.

Supplementary Information

The online version contains supplementary material available at https://doi.org/10.1186/s40478-025-02030-y.

Supplementary file 1

Acknowledgements
We gratefully acknowledge the selfless generosity of the brain donors and their families, facilitated by the University of Pennsylvania Center for Neurodegenerative Research, that made this research possible. We thank the Center for Advanced Magnetic Resonance Imaging and Spectroscopy at the University of Pennsylvania (RRID: SCR_022398) for their assistance with the acquisition of MRI data.

Author contributions

C.A., A.B., D.J.I., and P.A.Y. conceptualized the study and developed the methods. C.A., A.B., P.K., S.E., W.T., L.M.L., Z.K., D.T.O., E.T.B., N.C., S.S., S.A., S.A.L., K.P., R.I., J.L.R., T.S., E.B.L., M.D.T., S.R.D., D.A.W., D.J.I., and P.A.Y. performed research to acquire and process the data. C.A., P.K., and P.A.Y. analyzed the data and interpreted the results. C.A. drafted the initial manuscript and created the figures. All authors reviewed the manuscript and provided critical feedback. D.J.I. and P.A.Y. were the principal designers and coordinators of the study and supervised collection, analysis, and interpretation of the study data.

Funding
This work was supported by the US National Institutes of Health grants P30-AG072979, P01-AG066597, P01-AG084497, RF1-AG056014, and R01-AG069474.

Data availability

We will publish the code, scripts, and Jupyter notebooks closer to publication. The datasets generated and/or analyzed during the current study are not publicly available due to compliance and ethical reasons but are available from the corresponding author on reasonable request.

Declarations

Ethics Approval and Consent to Participate

Where possible, pre-consent during life and, in all cases, next-of-kin consent at death was given. Imaging studies were approved by the Institutional Review Board at the University of Pennsylvania and were in accordance with the Declaration of Helsinki.

Consent for Publication

All authors have reviewed the contents of the manuscript being submitted, approved of its contents, and validated the accuracy of the data and consented to publication.

Competing interests

D.A.W. has served as a paid consultant to Eli Lilly, GE Healthcare, and Qynapse. He serves on a Data Safety and Monitoring Board for Functional Neuromodulation and GSK. He is a site investigator for a clinical trial sponsored by Biogen. D.J.I. is a member of the science advisory board of Denali Therapeutics. S.R.D. received consultation fees from Rancho Biosciences and Nia Therapeutics. The other authors have nothing to disclose.

Received: 17 March 2025 Accepted: 5 May 2025

References

1. Dugger Brittany N, Dickson Dennis W (2017) Pathology of neurodegenerative diseases. Cold Spring Harb Perspect Biol. https://doi.org/10.1101/cshperspect.a028035
2. Clovis Foguem, Patrick Manckoundia (2018) Lewy body disease: clinical and pathological "Overlap syndrome" between synucleinopathies (Parkinson Disease) and tauopathies (Alzheimer Disease). Curr Neurol Neurosci Rep. https://doi.org/10.1007/s11910-018-0835-5
3. Mehta Rupal I, Schneider Julie A (2021) What Is 'Alzheimer's Disease'? the neuropathological heterogeneity of clinically defined Alzheimer's Dementia. Curr Opin Neurol. https://doi.org/10.1097/WCO.0000000000000912
4. Rabinovici Gil D et al (2017) Multiple comorbid neuropathologies in the setting of Alzheimer's disease neuropathology and implications for drug development. Alzheimer's Dement Transl Res Clin Interv. https://doi.org/10.1016/j.trci.2016.09.002
5. Ranjan Duara, Warren Barker (2022) Heterogeneity in Alzheimer's disease diagnosis and progression rates: implications for therapeutic trials. Neurotherapeutics. https://doi.org/10.1007/s13311-022-01185-z
6. Jack Clifford R et al (2018) NIA-AA research framework: toward a biological definition of Alzheimer's disease. Alzheimer's Dement J Alzheimer's Assoc. https://doi.org/10.1016/j.jalz.2018.02.018
7. Hu William T, Trojanowski John Q, Shaw Leslie M (2011) Biomarkers in Frontotemporal Lobar Degenerations—Progress and Challenges. Progress in Neurobiology. Biological Markers for Neurodegenerative Diseases. https://doi.org/10.1016/j.pneurobio.2011.04.012
8. Henchcliffe Claire, Dodel Richard, Beal M.Flint (2011) "Biomarkers of Parkinson's Disease and Dementia with Lewy Bodies". Progress in Neurobiology. Biological Markers for Neurodegenerative Diseases. https://doi.org/10.1016/j.pneurobio.2011.09.002
9. Nelson Peter T et al (2019) Limbic-predominant age-related TDP-43 encephalopathy (LATE): consensus working group report. Brain. https://doi.org/10.1093/brain/awz099
10. van Veluw Susanne J, Arfanakis Konstantinos, Julie A (2022) Schneider. Neuropathology of vascular brain health: insights from Ex vivo MRI-histopathology studies in cerebral small vessel disease. Stroke . https://doi.org/10.1161/STROKEAHA.121.032608
11. Dadar M et al (2024) The douglas-bell canada brain bank post-mortem brain imaging protocol. Aperture Neuro. https://doi.org/10.52294/001c.123347
12. Vonsattel JPG, del Amaya MP, Keller Christian E (2008) Twenty-first century brain banking. Processing brains for research: the Columbia university methods. Acta Neuropathol. https://doi.org/10.1007/s00401-007-0311-9
13. Sadhana Ravikumar et al (2021) Ex vivo MRI atlas of the human medial temporal lobe: characterizing neurodegeneration due to tau pathology. Acta Neuropathol Commun. https://doi.org/10.1186/s40478-021-01275-7
14. Denning Amanda E et al (2024) Association of quantitative histopathology measurements with antemortem medial temporal lobe cortical thickness in the Alzheimer's disease continuum. Acta Neuropathol. https://doi.org/10.1007/s00401-024-02789-9
15. David Lahna et al (2023) Postmortem 7T MRI for guided histopathology and evaluation of cerebrovascular disease. J Neuropathol Exp Neurol. https://doi.org/10.1093/jnen/nlac103
16. Yushkevich Paul A et al (2021) Three-dimensional mapping of neurofibrillary tangle burden in the human medial temporal lobe. Brain A J Neurol. https://doi.org/10.1093/brain/awab262
17. Young Peter NE et al (2020) Imaging biomarkers in neurodegeneration: current and future practices. Alzheimer's Res Therap. https://doi.org/10.1186/s13195-020-00612-7
18. Jonkman Laura E, Geurts Jeroen JG (2018) Chapter 23 - Postmortem Magnetic Resonance Imaging. Handbook of Clinical Neurology. In: Ingeborg Huitinga, Maree J. Webster. Brain Banking. Elsevier, https://doi.org/10.1016/B978-0-444-63639-3.00023-2
19. Matteo Mancini et al (2020) A multimodal computational pipeline for 3D histology of the human brain. Sci Rep. https://doi.org/10.1038/s41598-020-69163-z
20. Xiangrui Zeng et al (2024) Segmentation of supragranular and infragranular layers in ultra-high-resolution 7T Ex vivo MRI of the human cerebral cortex. Cereb Cortex. https://doi.org/10.1093/cercor/bhae362

21. Jagust William J et al (2008) Neuropathological basis of magnetic resonance images in aging and dementia. Ann Neurol. https://doi.org/10.1002/ana.21296
22. Das Sandhitsu R et al (2021) Application of histopathologically derived 3D tau burden map as in-vivo region of interest for biomarker analysis. Alzheimer's Dement. https://doi.org/10.1002/alz.055096
23. Burke Sarah E et al (2022) Phases of volume loss in patients with known frontotemporal lobar degeneration spectrum pathology. Neurobiol Aging. https://doi.org/10.1016/j.neurobiolaging.2022.02.007
24. Min Chen et al (2023) Antemortem network analysis of spreading pathology in autopsy-confirmed frontotemporal degeneration. Brain Commun. https://doi.org/10.1093/braincomms/fcad147
25. Giannini Lucia AA et al (2019) Divergent patterns of TDP-43 and Tau pathologies in primary progressive aphasia. Ann Neurol. https://doi.org/10.1002/ana.25465
26. Irwin David J et al (2018) Asymmetry of post-mortem neuropathology in behavioural-variant frontotemporal dementia. Brain. https://doi.org/10.1093/brain/awx319
27. Olm Christopher A et al (2023) Event-Based Modeling of T1-weighted MRI Is Related to Pathology in Frontotemporal Lobar Degeneration Due to Tau and TDP. Clinical, NeuroImage. https://doi.org/10.1016/j.nicl.2022.103285
28. Shokufeh Sadaghiani et al (2023) Associations of phosphorylated Tau pathology with whole-hemisphere ex vivo morphometry in 7 tesla MRI. Alzheimer's Dement. https://doi.org/10.1002/alz.12884
29. Dylan Tisdall M et al (2022) Ex vivo MRI and histopathology detect novel iron-rich cortical inflammation in frontotemporal lobar degeneration with tau versus TDP-43 pathology. Clinical, NeuroImage. https://doi.org/10.1016/j.nicl.2021.102913
30. Jonkman Laura E et al (2019) Post-mortem MRI and histopathology in neurologic disease: a translational approach. Neurosci Bull. https://doi.org/10.1007/s12264-019-00342-3
31. Adrià Casamitjana et al (2024) A next-generation. Histol Atlas Hum Brain Appl Autom Brain MRI Segm. https://doi.org/10.1101/2024.02.05.579016
32. Pichat J et al (2017) Part-to-whole registration of histology and MRI using shape elements. In: Proceedings of the IEEE international conference on computer vision workshops. pp 107–115
33. Katrin Amunts et al (2013) BigBrain: an ultrahigh-resolution 3D human brain model. Science. https://doi.org/10.1126/science.1235381
34. Adrià Casamitjana et al (2022) Robust joint registration of multiple stains and mri for multimodal 3D histology reconstruction: application to the allen human brain atlas. Med Image Anal. https://doi.org/10.1016/j.media.2021.102265
35. Jonas Pichat et al (2018) A survey of methods for 3D histology reconstruction. Med Image Anal. https://doi.org/10.1016/j.media.2018.02.004
36. Danner Benjamin et al (2024) Brain banking in the united states and europe: importance, challenges, and future trends. J Neuropathol Exp Neurol. https://doi.org/10.1093/jnen/nlae014
37. Bennett David A et al (2018) Religious orders study and rush memory and aging project. J Alzheimer's Dis JAD. https://doi.org/10.3233/JAD-179939
38. Montine Thomas J et al (2012) National institute on aging-Alzheimer's association guidelines for the neuropathologic assessment of Alzheimer's disease: a practical approach. Acta Neuropathol. https://doi.org/10.1007/s00401-011-0910-3
39. Toledo Jon B et al (2014) A platform for discovery: the university of pennsylvania integrated neurodegenerative disease biobank. Alzheimer's Dement. https://doi.org/10.1016/j.jalz.2013.06.003
40. Pulkit Khandelwal et al (2024) Automated deep learning segmentation of high-resolution 7 tesla postmortem mri for quantitative analysis of structure-pathology correlations in neurodegenerative diseases. Imaging Neurosci. https://doi.org/10.1162/imag_a_00171
41. Hyman Bradley T et al (2012) National institute on aging-alzheimer's association guidelines for the neuropathologic assessment of Alzheimer's disease. Alzheimer's Dement J Alzheimer's Assoc. https://doi.org/10.1016/j.jalz.2011.10.007
42. Yushkevich Paul A et al (2019) User-guided segmentation of multi-modality medical imaging datasets with ITK-SNAP. Neuroinformatics. https://doi.org/10.1007/s12021-018-9385-x
43. Yushkevich Paul A et al (2006) User-guided 3D active contour segmentation of anatomical structures: significantly improved efficiency and reliability. Neuroimage. https://doi.org/10.1016/j.neuroimage.2006.01.015
44. Sadhana Ravikumar et al (2024) Postmortem imaging reveals patterns of medial temporal lobe vulnerability to tau pathology in Alzheimer's disease. Nat Commun. https://doi.org/10.1038/s41467-024-49205-0
45. Heinrich Mattias P et al (2012) MIND: Modality Independent Neighbourhood Descriptor for Multi-Modal Deformable Registration". Medical Image Analysis. Special Issue on the 2011 Conference on Medical Image Computing and Computer Assisted Intervention . https://doi.org/10.1016/j.media.2012.05.008
46. Yushan Zheng et al (2019) Adaptive color deconvolution for histological WSI normalization. Comput Methods Programs Biomed. https://doi.org/10.1016/j.cmpb.2019.01.008
47. Pielawski N et al (2020) CoMIR: contrastive multimodal image representation for registration. Adv Neural Inform Proces Syst
48. Karypis G, Kumar V (1997) METIS: a software package for partitioning unstructured graphs, partitioning meshes, and computing fill-reducing orderings of sparse matrices. University Digial Conservancy . https://hdl.handle.net/11299/215346
49. Durand Thibaut et al (2017) WILDCAT: weakly supervised learning of deep convnets for image classification, pointwise localization and segmentation. In: Proceedings of the IEEE conference on computer vision and pattern recognition
50. Ronneberger O, Fischer P, Brox T (2015) U-Net: convolutional networks for biomedical image segmentation. medical image computing and computer-assisted intervention - MICCAI 2015. https://doi.org/10.1007/978-3-319-24574-4_28
51. Caselles V, Kimmel R, Sapiro G (1997) Geodesic active contours. Int J Comput Vis. https://doi.org/10.1023/A:1007979827043
52. Ogniewicz R, Ilg M (1992) Voronoi skeletons: theory and applications. In: Proceedings 1992 IEEE computer society conference on computer vision and pattern recognition. https://doi.org/10.1109/CVPR.1992.223226
53. Khandelwal P et al (2024) Surface-based parcellation and vertex-wise analysis of ultra high-resolution ex vivo 7 tesla MRI in Alzheimer's disease and related dementias. https://doi.org/10.48550/arXiv.2403.19497
54. Desikan Rahul S et al (2006) An automated labeling system for subdividing the human cerebral cortex on MRI scans into gyral based regions of interest. Neuroimage. https://doi.org/10.1016/j.neuroimage.2006.01.021
55. Fischl B et al (1999) High-Resolution Intersubject Averaging and a Coordinate System for the Cortical Surface. Human Brain Mapping. https://doi.org/10.1002/(sici)1097-0193(1999)8:4<272::aid-hbm10>3.0.co;2-4
56. Smith Stephen M, Nichols Thomas E (2009) Threshold-Free Cluster Enhancement: Addressing Problems of Smoothing, Threshold Dependence and Localisation in Cluster Inference. NeuroImage. https://doi.org/10.1016/j.neuroimage.2008.03.061
57. Nichols T, Hayasaka S (2003) Controlling the familywise error rate in functional neuroimaging: a comparative review. Stat Methods Med Res. https://doi.org/10.1191/0962280203sm341ra
58. Winkler AM, Ridgway GR, Webster MA, Smith SM, Nichols TE (2014) Permutation inference for the general linear model. NeuroImage. https://doi.org/10.1016/j.neuroimage.2014.01.060
59. Alex Wesseling et al (2023) Amygdala volume as neuroimaging marker of limbic-predominant age-related TDP-43 encephalopathy (LATE) in neurodegenerative disease: a post-mortem MRI and pathology study. Alzheimer's Dement. https://doi.org/10.1002/alz.083090
60. Wisse LEM et al (2021) Downstream effects of polypathology on neurodegeneration of medial temporal lobe subregions. Acta Neuropathol Commun. https://doi.org/10.1186/s40478-021-01225-3
61. Dickerson Bradford C et al (2009) The Cortical Signature of Alzheimer's Disease: Regionally Specific Cortical Thinning Relates to Symptom Severity in Very Mild to Mild AD Dementia and Is Detectable in Asymptomatic Amyloid-Positive Individuals. Cerebral Cortex (New York, NY). https://doi.org/10.1093/cercor/bhn113
62. Dawe Robert J et al (2011) Neuropathologic correlates of hippocampal atrophy in the elderly: a clinical. PLoS ONE, Pathologic, Postmortem MRI Study. https://doi.org/10.1371/journal.pone.0026286
63. Teresa Gómez-Isla et al (1997) Neuronal loss correlates with but exceeds neurofibrillary tangles in Alzheimer's disease. Ann Neurol. https://doi.org/10.1002/ana.410410106
64. Ohm Daniel T et al (2021) Accumulation of neurofibrillary tangles and activated microglia is associated with lower neuron densities in the aphasic variant of Alzheimer's Disease. Brain Pathol. https://doi.org/10.1111/bpa.12902

65. Vizcarra JC et al (2023) Survey of neuroanatomic sampling and staining procedures in Alzheimer disease research center brain banks. Free Neuropathol. https://doi.org/10.17879/freeneuropathology-2023-4696
66. Baldi D et al (2019) MR imaging-histology correlation by tailored 3d-printed slicer in oncological assessment. Contrast Media Mol Imaging. https://doi.org/10.1155/2019/1071453
67. Boopathy Jegathambal Sethu K, et al (2018) MRI Based Brain-Specific 3D-Printed Model Aligned to Stereotactic Space for Registering Histology to MRI. In: 2018 40th annual international conference of the IEEE engineering in medicine and biology society (EMBC).. https://doi.org/10.1109/EMBC.2018.8512346
68. Martina Absinta et al (2014) Postmortem magnetic resonance imaging to guide the pathological cut: individualized, 3D-printed cutting boxes for fixed brains. J Neuropathol Exp Neurol. https://doi.org/10.1097/NEN.0000000000000096
69. Liou Jr-Jiun et al (2024) Correlating hippocampal and amygdala volumes with neuropathological burden in neurodegenerative diseases using 7T postmortem MRI. https://doi.org/10.1101/2024.05.15.24307354
70. Bö L et al (2004) Magnetic resonance imaging as a tool to examine the neuropathology of multiple sclerosis. Neuropathol Appl Neurobiol. https://doi.org/10.1111/j.1365-2990.2003.00521.x
71. Silbert Lisa C et al (2024) White matter hyperintensities and the surrounding normal appearing white matter are associated with water channel disruption in the oldest old. Alzheimer's Dement. https://doi.org/10.1002/alz.13816
72. Frigerio Irene et al (2021) Amyloid-β, p-Tau and reactive microglia are pathological correlates of MRI cortical atrophy in Alzheimer's disease. Brain Commun. https://doi.org/10.1093/braincomms/fcab281
73. Bulk Marjolein et al (2018) Postmortem MRI and histology demonstrate differential iron accumulation and cortical myelin organization in early- and late-onset Alzheimer's disease. Neurobiol Aging. https://doi.org/10.1016/j.neurobiolaging.2017.10.017
74. Meadowcroft Mark D et al (2009) MRI and histological analysis of beta-amyloid plaques in both human Alzheimer's disease and APP/PS1 transgenic mice. J Magn Reson Imaging. https://doi.org/10.1002/jmri.21731
75. Klaus Schmierer et al (2004) Magnetization Transfer Ratio and Myelin in Postmortem Multiple Sclerosis Brain. Ann Neurol. https://doi.org/10.1002/ana.20202
76. Nag S et al (2021) Ex Vivo MRI Facilitates Localization of Cerebral Microbleeds of Different Ages during Neuropathology Assessment. Free Neuropathol. https://doi.org/10.17879/freeneuropathology-2021-3638
77. Poole Victoria N et al (2024) Associations of brain morphology with cortical proteins of cognitive resilience. Neurobiol Aging. https://doi.org/10.1016/j.neurobiolaging.2024.02.005
78. Lei Yu et al (2020) Contribution of TDP and hippocampal sclerosis to hippocampal volume loss in older-old persons. Neurology. https://doi.org/10.1212/WNL.0000000000008679
79. Konstantinos Arfanakis et al (2020) Neuropathologic correlates of white matter hyperintensities in a community-based cohort of older adults. J Alzheimer's Dis JAD. https://doi.org/10.3233/JAD-190687
80. Kapasi Alifiya et al (2023) High-throughput digital quantification of alzheimer disease pathology and associated infrastructure in large autopsy studies. J Neuropathol Exp Neurol. https://doi.org/10.1093/jnen/nlad086
81. Kristin Gellein et al (2008) Leaching of trace elements from biological tissue by formalin fixation. Biol Trace Elem Res. https://doi.org/10.1007/s12011-007-8051-1
82. Matsuo ES et al (1994) Biopsy-derived adult human brain Tau is phosphorylated at many of the same sites as Alzheimer's Disease paired helical filament Tau. Neuron. https://doi.org/10.1016/0896-6273(94)90264-x
83. Blair Jeffrey A et al (2016) Individual case analysis of postmortem interval time on brain tissue preservation. PLoS ONE. https://doi.org/10.1371/journal.pone.0151615
84. Iana Lesnikova et al (2018) Usability of immunohistochemistry in forensic samples with varying decomposition. Am J Forensic Med Pathol. https://doi.org/10.1097/PAF.0000000000000408

Publisher's Note